CHAPTER 3

ADVANCED ESR SPECTROSCOPY IN MEMBRANE BIOPHYSICS

Janez Štrancar
EPR Center, Laboratory of Biophysics,
"Jožef Stefan" Institute, Ljubljana, Slovenia

1. INTRODUCTION

1.1. Biophysical Background

Our current knowledge about **biological membranes** shows that they belong to the most important cell structures. Mass transport and signal transduction obviously appear to be vital to physiological functions of biomembranes as they enable cellular compartmentalization and control over it at the same time. Many experiments and theoretical considerations in the past decades have shown that membranes consist of a laterally heterogeneous lipid bilayer with a large number of different protein molecules embedded in the lipid bilayer. Heterogeneity exists at any level — from the biochemical to the physical level, meaning that different constituents and supramolecular structures in membranes interact via different interactions and exhibit different motional characteristics. This complexity — as the most striking property of any biological system — remains a tough problem also for the up-to-date experimental and theoretical approaches.

As will be shown in this chapter, recent developments in **electron spin resonance spectroscopy (ESR)** bring new possibilities to the further exploration of biosystems.

> The appropriateness of the ESR nanosecond time window and its sensitivity make **spin-label ESR** one of the most informative techniques, able to resolve the puzzle of membrane heterogeneity and intermolecular interactions as well as its role in cell signaling and mass transport.

Recent numerical approaches in combination with spin-label ESR experiments allow characterization of coexisting membrane structures in the cases of specific labeling as well as for nonspecific labeling, resulting in extremely valuable information about living structures in their native environment with only the small perturbation of the addition of spin probes.

Fast spectral simulation algorithms valid for physiological conditions, hybrid evolutionary optimization techniques responsible for efficient inverse-problem solving, and good solution-condensation algorithms have evolved spin-label ESR into an even more powerful technique for studying the dynamics and structure–function relationship of coexisting membrane constituents, like membrane lipid domains, carbohydrate surface aggregates, and conformational freedom of membrane peptides and proteins.

The aim of this chapter is therefore to present the key steps involved in this membrane characterization procedure and that can be applied as more general principles for any form of spectroscopy:

- Motional averaging in a spin-labeled biomembrane
- Strategies for calculating powder spectra
- Solving an inverse problem and condensation of the results

In the characterization procedure all the important properties of the experiment should be built into the simulation model. Furthermore, all the relevant characteristics of the model should enable a valuable characterization of the system within a reasonable time. To make a characterization procedure a useful tool in membrane biophysics as well as in more general cases, the following **three important requirements** need to be considered:

- Simulation should take into account all important characteristics of the ESR experiment and the complexity of the biological system
- Simulation should be fast enough to allow application of a robust scheme for inverse problem solving
- Simulation should be accurate enough to be sensitive to physiological changes

1.2. Mathematical Background

To clarify the notation of the various mathematical symbols and operations, they are introduced here briefly.

A **vector quantity** will be denoted by a one-sided arrow, e.g., magnetic field $\vec{B}$. In case of a **unit vector** with a length of 1, it will be stressed by a double-sided arrow, e.g., the unit vector of a coordinate system $\overleftrightarrow{x}$. A **tensor** quantity will be indicated by an underline, e.g., $\underline{A}$, a **unit tensor** (with diagonal elements 1 and off-diagonal elements 0) by $\underline{1}$. **Scalar products** between vectors, between a vector and matrices, and between matrices will be shown without a dot:

$$
\begin{gathered}
\vec{B}\;\vec{S}=\begin{pmatrix} B_x & B_y & B_z \end{pmatrix}\begin{pmatrix} S_x \\ S_y \\ S_z \end{pmatrix}=B_xS_x+B_yS_y+B_zS_z,\\
\vec{B}\;\underline{g}=\begin{pmatrix} g_{xx} & g_{xy} & g_{xz} \\ g_{yx} & g_{yy} & g_{yz} \\ g_{zx} & g_{zy} & g_{zz} \end{pmatrix}\begin{pmatrix} S_x \\ S_y \\ S_z \end{pmatrix}=\begin{pmatrix} g_{xx}S_x+g_{xy}S_y+g_{xz}S_z \\ g_{yx}S_x+g_{yy}S_y+g_{yz}S_z \\ g_{zx}S_x+g_{zy}S_y+g_{zz}S_z \end{pmatrix},\\
\underline{R}\;\underline{P}=\begin{pmatrix} R_{xx} & R_{xy} & R_{xz} \\ R_{yx} & R_{yy} & R_{yz} \\ R_{zx} & R_{zy} & R_{zz} \end{pmatrix}\begin{pmatrix} P_{xx} & P_{xy} & P_{xz} \\ P_{yx} & P_{yy} & P_{yz} \\ P_{zx} & P_{zy} & P_{zz} \end{pmatrix}\\
=\begin{pmatrix} R_{xx}P_{xx}+R_{xy}P_{yx}+R_{xz}P_{zx} & R_{xx}P_{xy}+R_{xy}P_{yy}+R_{xz}P_{zy} & R_{xx}P_{xz}+R_{xy}P_{yz}+R_{xz}P_{zz} \\ R_{yx}P_{xx}+R_{yy}P_{yx}+R_{yz}P_{zx} & R_{yx}P_{xy}+R_{yy}P_{yy}+R_{yz}P_{zy} & R_{yx}P_{xz}+R_{yy}P_{yz}+R_{yz}P_{zz} \\ R_{zx}P_{xx}+R_{zy}P_{yx}+R_{zz}P_{zx} & R_{zx}P_{xy}+R_{zy}P_{yy}+R_{zz}P_{zy} & R_{zx}P_{xz}+R_{zy}P_{yz}+R_{zz}P_{zz} \end{pmatrix}.
\end{gathered}
\tag{1}
$$

Operators will be indicated with a circumflex accent sign, e.g., scalar operator $\hat{H}$ and vector operator $\hat{\vec{S}}$.

Time and ensemble average are denoted as $\overline{f}$ and $\langle f\rangle$, respectively.

Angles will be denoted by Greek letters.

Indication of the coordinate system (l), where a vector or a tensor quantity X is well defined, it will be explicitly expressed by the left-upper index, e.g., ${}^{(l)}X$. When applied, it should remind the reader of a base of this coordinate system, defined through a set of unit vectors: ${}^{(l)}\mathcal{B}=\left\{{}^{(l)}\vec{i},\ {}^{(l)}\vec{j},\ {}^{(l)}\vec{k}\right\}$.

In membrane spectroscopy four important coordinate systems are relevant:

- Nitroxide molecular coordinate system (n)
- Membrane coordinate system (m)
- Laboratory coordinate system (l)
- Coordinate system of local magnetic field (lm)

The introduction of these coordinate systems originates in the fact that various physical quantities can be well defined only in one of these coordinate systems. This is indicated in the following list of quantities and coordinate systems in which these quantities are well defined.

According to the properties above, the bases of the coordinate systems can be defined as indicated in Table 2 and Figure 1.

Coordinate systems *(a)* and *(b)* can be connected by means of **unitary transformation** R, denoted by $R\equiv R^{(a)\to(b)}:{}^{(a)}\mathcal{B}\to{}^{(b)}\mathcal{B}$. The inverse transformation is denoted by a complex conjugate (real transposed) $R^{(a)\to(b)}$. Generally, a unitary transformation $R^{(a)\to(b)}$ can be expressed by three consequent rotations $R_{z''}^{(a'')\to(b)}(\varphi)\,R_{y'}^{(a')\to(a'')}(\vartheta)\,R_{z}^{(a)\to(a')}(\psi)$ about a temporary z-, y'-, or z''-axis (see Eq. (2)).

Table 1. Coordinate Systems with Well-Defined Quantities

Quantity Q	Coordinate system, in which Q is well defined
External magnetic field B	Laboratory coordinate system *(l)*
Local magnetic field B^l	Local magnetic field coordinate system *(lm)*
Electron spin S	Local magnetic field coordinate system *(lm)*
Nuclear spin I	Local magnetic field coordinate system *(lm)*
Zeeman tensor g	Nitroxide (molecular) coordinate system *(n)*
Hyperfine tensor A	Nitroxide (molecular) coordinate system *(n)*
Membrane normal n	Membrane coordinate system *(m)*

Table 2. Definition of Coordinate Systems

Coordinate system (cs)	Definition of base
Nitroxide (molecular) cs *(n)*	x-axis parallel to NO bond, z-axis parallel to π orbital
Membrane cs *(m)*	z-axis parallel to membrane normal
Laboratory cs *(l)*	z-axis parallel to external magnetic field
Local magnetic field cs *(lm)*	z-axis parallel to local magnetic field ${}^{(lm)}\vec{B} = {}^{(n)}\underline{g}\,{}^{(l)}\vec{B}$

$$R^{(a)\to(b)} = \begin{pmatrix} \cos\varphi & \sin\varphi & 0 \\ -\sin\varphi & \cos\varphi & 0 \\ 0 & 0 & 1 \end{pmatrix} \begin{pmatrix} \cos\vartheta & 0 & \sin\vartheta \\ 0 & 1 & 0 \\ -\sin\vartheta & 0 & \cos\vartheta \end{pmatrix} \begin{pmatrix} \cos\psi & \sin\psi & 0 \\ -\sin\psi & \cos\psi & 0 \\ 0 & 0 & 1 \end{pmatrix}. \tag{2}$$

In case of the coordinate systems mentioned previously, the unitary transformations are presented in Figure 2. **Transformation matrices** are derived by application of Euler rotation matrices as indicated above:

- For transformation from the laboratory to the membrane coordinate system (the first rotation around the z-axis in the laboratory coordinate system is omitted, since the Hamiltonian is invariant to a rotation around an external magnetic field axis):

$$R^{(l)\to(m)} = \begin{pmatrix} \cos\Phi & \sin\Phi & 0 \\ -\sin\Phi & \cos\Phi & 0 \\ 0 & 0 & 1 \end{pmatrix} \begin{pmatrix} \cos\Theta & 0 & \sin\Theta \\ 0 & 1 & 0 \\ -\sin\Theta & 0 & \cos\Theta \end{pmatrix}. \tag{3}$$

- For transformation from the membrane to the nitroxide coordinate system:

$$R^{(m)\to(n)} = \begin{pmatrix} \cos\varphi & \sin\varphi & 0 \\ -\sin\varphi & \cos\varphi & 0 \\ 0 & 0 & 1 \end{pmatrix} \begin{pmatrix} \cos\vartheta & 0 & \sin\vartheta \\ 0 & 1 & 0 \\ -\sin\vartheta & 0 & \cos\vartheta \end{pmatrix} \begin{pmatrix} \cos\psi & \sin\psi & 0 \\ -\sin\psi & \cos\psi & 0 \\ 0 & 0 & 1 \end{pmatrix}. \quad (4)$$

- For transformation from the laboratory to the local magnetic field coordinate system and vice versa

$$R^{(l)\to(lm)} = \frac{\overline{R^{(l)\to(m)}}\ \ \overline{R^{(m)\to(n)}}\ \ g\ \ R^{(m)\to(n)}\ \ R^{(l)\to(m)}}{\left|\overline{R^{(l)\to(m)}}\ \ \overline{R^{(m)\to(n)}}\ \ g\ \ R^{(m)\to(n)}\ \ R^{(l)\to(m)}\ \ {}^{(l)}\vec{k}\right|}, \quad (5)$$

$$\begin{aligned} R^{(lm)\to(l)} = {} & \left|\overline{R^{(l)\to(m)}}\ \ \overline{R^{(m)\to(n)}}\ \ g\ \ R^{(m)\to(n)}\ \ R^{(l)\to(m)}\ \ {}^{(l)}\vec{k}\right| \\ & \overline{R^{(l)\to(m)}}\ \ \overline{R^{(m)\to(n)}}\ \ g^{-1}\ \ R^{(m)\to(n)}\ \ R^{(l)\to(m)}. \end{aligned} \quad (6)$$

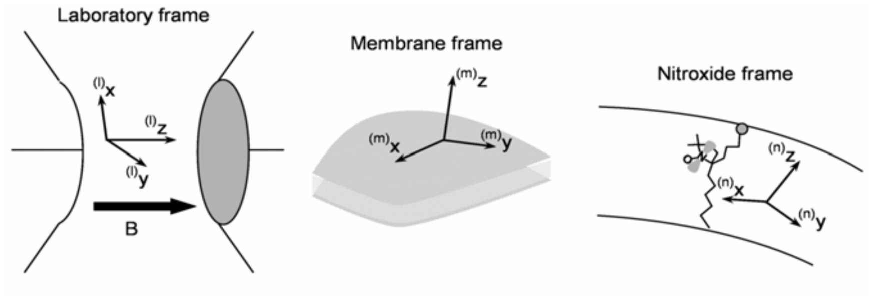

Figure 1. Schematic presentation of the coordinate systems.

1.3. Quantum-Physical Background

To follow this chapter, the reader should be familiar with basic operations of quantum physics, i.e., working with operators and calculating eigenvalues of the spin operators as well as of the Hamiltonian operator. It is not the aim of this chapter to teach the basics of quantum physics; however, for the sake of clarity we briefly review the basic principles.

If the system state is described by a single set of quantum numbers $\{\xi\}$, or shortly in Dirac bracket notation $|\xi\rangle$, then its eigenvalue (eigenenergy) E_ξ can be calculated by application of a Hamiltonian operator function in the following way:

$$\hat{H}|\xi\rangle = E_\xi|\xi\rangle \to E_\xi = \frac{\langle\xi|\hat{H}|\xi\rangle}{\langle\xi|\xi\rangle} \xrightarrow{\langle\xi|\xi\rangle=1} E_\xi = \langle\xi|\hat{H}|\xi\rangle. \quad (1)$$

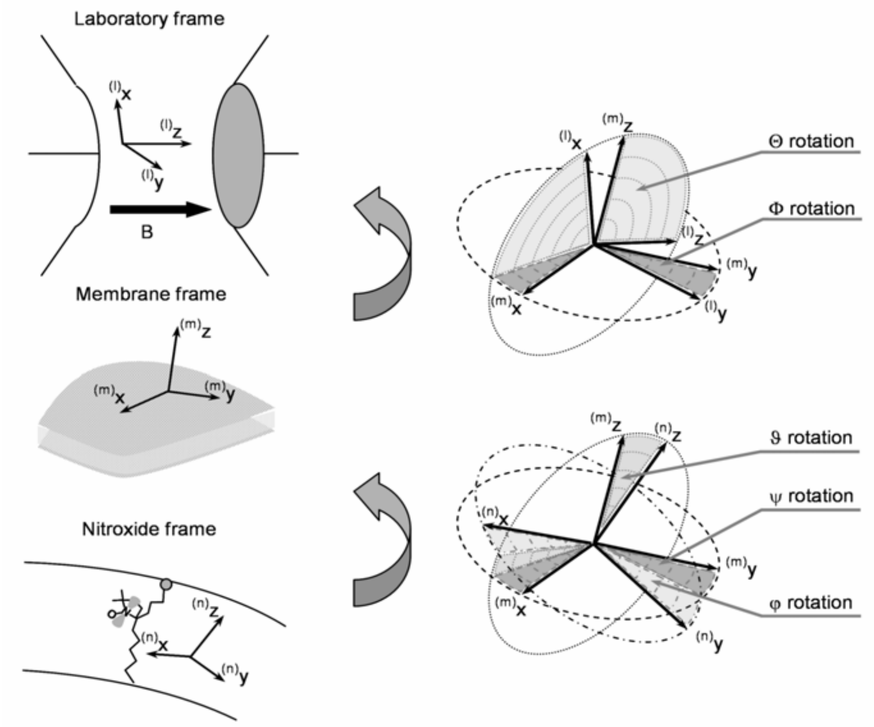

Figure 2. Schematic presentation of the transformations between coordinate systems using Euler rotations.

However, usually there are N states $|\xi_i\rangle$ allowed in a real system. In such a case the eigenvalues (eigenenergies) should be calculated as the principal values of the Hamiltonian matrix defined as

$$\underline{E} = \begin{pmatrix} E_{11} & \cdots & E_{1N} \\ \vdots & \ddots & \vdots \\ E_{N1} & \cdots & E_{NN} \end{pmatrix} \leftarrow E_{ij} = \langle \xi_i | \hat{H} | \xi_j \rangle . \tag{2}$$

Since ESR spectroscopy involves the transition of spin states, the Hamiltonian operator includes the spin operators. Consequently, one should be familiar with the basics of spin algebra. In case of nitroxide spin labels, the spin states of the electron spin, $S = ½$, and nitrogen nuclear spin of $I = 1$ are involved, implying the usage of the following set of base functions:

$$\{ |M_S, M_I\rangle \} = \{ |\tfrac{1}{2},1\rangle, |-\tfrac{1}{2},1\rangle, |\tfrac{1}{2},0\rangle, |-\tfrac{1}{2},0\rangle, |\tfrac{1}{2},-1\rangle, |-\tfrac{1}{2},-1\rangle \} . \tag{3}$$

Here, the short notation of base functions $\left|M_S, M_I\right\rangle$ is used instead of $\left|S, M_S, I, M_I\right\rangle$. The basic rules of spin algebra and the eigenvalues of the various spin operators are

$$\begin{aligned}
&\hat{S}_z\left|S, M_S, I, M_I\right\rangle = M_S\left|S, M_S, I, M_I\right\rangle,\\
&\hat{S}_{\pm}\left|S, M_S, I, M_I\right\rangle = \sqrt{\left(S \mp M_S\right)\left(S \pm M_S + 1\right)}\left|S, M_S \pm 1, I, M_I\right\rangle,\\
&\hat{I}_z\left|S, M_S, I, M_I\right\rangle = M_I\left|S, M_S, I, M_I\right\rangle,\\
&\hat{I}_{\pm}\left|S, M_S, I, M_I\right\rangle = \sqrt{\left(I \mp M_I\right)\left(I \pm M_I + 1\right)}\left|S, M_S, I, M_I \pm 1\right\rangle,\\
&\left\langle S, M_S, I, M_I \middle| S, M_S', I, M_I'\right\rangle = \delta_{M_S, M_S'}\delta_{M_I, M_I'}.
\end{aligned} \tag{10}$$

Expansion of the vector spin operator in the basis of the coordinate system of the local magnetic field can be written in the following form:

$$\begin{aligned}
\hat{\vec{S}} &= \hat{S}_x\ \vec{i} + \hat{S}_y\ \vec{j} + \hat{S}_z\ \vec{k}\\
&= \tfrac{1}{2}\left(\hat{S}^{+} + \hat{S}^{-}\right)\ \vec{i} + \tfrac{1}{2i}\left(\hat{S}^{+} - \hat{S}^{-}\right)\ \vec{j} + \hat{S}_z\ \vec{k}.
\end{aligned} \tag{11}$$

2. MOTIONAL AVERAGING IN A SPIN-LABELED BIOMEMBRANE

2.1. Spin Labeling Experiment

To be able to detect an ESR spectrum, a stable unpaired-electron system should be part of the system or introduced into the system.

A spin labeling experiment involves implementation of **nitroxide-based spin probes**.

Usually, introduction of a spin probe is a **nonspecific addition of spin-labeled analogs of common biomolecules** that can be found in biomembranes (or other biosystems). The nitroxide group, which contains a stable free radical, can be attached at different positions of a molecule. If a nitroxide moiety can be justified as a small perturbation to a (larger) biomolecule or supramolecular structure, then the partitioning properties of a spin-labeled molecule are very similar to the partitioning properties of the original molecules — a property that can be used for subsystem identification.

On the other hand, a spin label can be introduced into a biosystem also in a **specific** manner, using a biochemical **targeting** procedure. In this case, its position is well defined, and the complexity that is determined from spectral simulation directly points to local conformations of the targeted biomolecule. Since the presented approach can be used also to detect conformations at nonspecific sites, special care should be taken to identify all possible binding sites and to include the reaction rates of nitroxide binding to these sites.

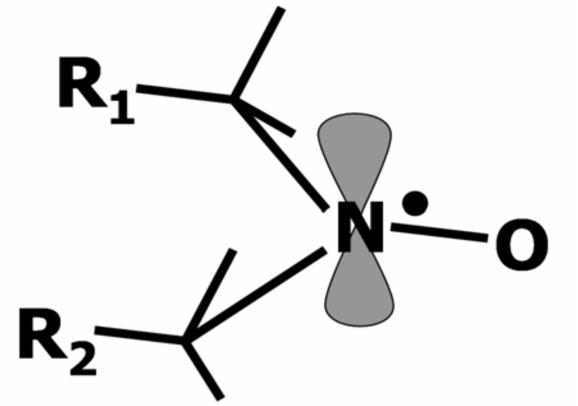

Figure 3. Nitroxide group.

If physiologically relevant information should be detected, the **temperature** of a spin-label experiment should be chosen in quite a narrow interval. Note that "physiological temperature" depends on the biological species, e.g., 0–50°C for various bacteria, 37°C for mammalians, etc. At such temperatures organisms react on a millisecond timescale, and local biosignaling processes on biomembranes occur on the ten microseconds timescale. The local dynamics of the membrane constituents should be fast enough to enable lipid or protein supramolecular structures to find their favored state within this timeframe. Global conformational changes that are involved in biosignaling should evolve through reconfiguration over several thousand of conformational states. That can only be achieved with fast local molecular motions with correlation times at the sub-nanosecond timescale. This fact is confirmed by many molecular dynamics simulations and strongly influences the modeling scheme of the ESR spectral simulations for physiological temperatures.

Physiological temperatures involve rotational motion on the nanosecond timescale, which is fast on the ESR timescale. This implies partial averaging of the nitroxide magnetic properties over the allowed local rotational configurations. Additional slower time evolution of labeled subsystems will be determined as coexisting motional/polarity patterns.

However, some ESR experiments cannot be performed at physiological temperatures. When a much lower temperature has to be used, slow rotational motions come into play. To simulate such experiments one has to implement slow-motion schemes. However, one has to be aware of the fact that the resulting anisotropy of the system and rate of rotational motion in the slow-motion ESR regime create a numerically ill-posed problem, i.e., in complex membrane systems and cell suspensions, the anisotropy and rate of rotational motion cannot be distinguished well enough.

2.2. The Hamiltonian for Spin Labels

The spin Hamiltonian of a nitroxide spin label can be approximated by a combination of a **Zeeman term** (interaction between electron spin *S* and external magnetic field *B*) and a **hyperfine term** (interaction between electron spin *S* and nitrogen nuclear spin *I*):

$$\hat{H} = \mu_B \vec{B}\ \underline{g}\ \ \hat{\vec{S}} + \hat{\vec{I}}\,\underline{A}\ \ \hat{\vec{S}}\,. \tag{12}$$

The superhyperfine interaction between the electron spin and neighboring proton spins can be effectively taken into account in the linewidth calculation by an additional broadening. The nuclear Zeeman interaction between the nuclear spins and the magnetic field are neglected due to (latter) application of selection rules, which imply transitions to occur between electron spin states and not between nuclear spin states.

Different quantities in Hamiltonian equation (12) are well defined only in their own coordinate system (see Tables 1 and 2).

To explicitly express the coordinate systems in which the quantities are well defined, we can use the notation defined in the §1 and identify the coordinate systems according to their indices. Remember that the magnetic properties are well defined in the nitroxide molecular system *(n)*, the external magnetic field in the laboratory system *(l)*, and the spin operators in the coordinate system of the local magnetic field *(lm)*. Note that the usage of simple spin algebra is limited to the coordinate system where the direction of quantization is known, which is the case only for the coordinate system of the local magnetic field *(lm)*:

$$\hat{H} = \mu_B\, {}^{(l)}\vec{B}\ \ {}^{(n)}\underline{g}\ \ {}^{(lm)}\hat{\vec{S}} + {}^{(lm)}\hat{\vec{I}}\ \ {}^{(n)}\underline{A}\ \ {}^{(lm)}\hat{\vec{S}}\,. \tag{13}$$

Although the Hamiltonian expression does not depend on the choice of coordinate system, one has to express all the quantities in the same coordinate system to solve the eigensystem equation. Therefore one should introduce transformation matrices between the quantities defined in different coordination systems. Consequently, the Hamiltonian for a single spin probe molecule should be rewritten as

$$\hat{H} = \mu_B \vec{B}\ \ \overline{R^{(l)\to(n)}}\ \underline{g}\ R^{(lm)\to(n)}\ \ \hat{\vec{S}}\ +\ \hat{\vec{I}}\ \ \overline{R^{(lm)\to(n)}}\ \underline{A}\ \ R^{(lm)\to(n)}\hat{\vec{S}}\,. \tag{14}$$

Since the ESR experiment involves several spin probe molecules, actually more than 10^{13}, which is the sensitivity limit for a nitroxide spin-label experiment on the current ESR spectrometers, Eq. (14) actually becomes

$$\hat{H} = \sum_i \left[\mu_B \vec{B}\ \overline{R_i^{(l)\to(n)}}\ \underline{g}\ R_i^{(lm)\to(n)}\ \hat{\vec{S}} + \hat{\vec{I}}\ \overline{R_i^{(lm)\to(n)}}\ \underline{A}\ R_i^{(lm)\to(n)} \hat{\vec{S}} \right]. \tag{15}$$

Note that summation over the nitroxide molecules includes summation over their different orientations; however, the electron and nuclear spin states are equivalent for all spin probes. The same is valid for the magnetic properties of the spin probes. Orientational dependencies are buried within the transformation matrices.

Introducing the transformation to and from the coordinate system of the local magnetic field as given by Eqs. (5) and (6), the **Zeeman term** of Eq. (14) becomes

$$\hat{H}_{\text{Zeeman}} = \mu_B B\ \left| \overline{R^{(l)\to(m)}}\ \overline{R^{(m)\to(n)}}\ \underline{g}\ R^{(m)\to(n)}\ R^{(l)\to(m)}\ \vec{k} \right|\ \vec{k}\ \hat{\vec{S}}. \tag{16}$$

By expanding the vector spin operator in the basis of the local magnetic field coordinate system as shown in Eq. (11), the Zeeman term can be simplified to

$$\hat{H}_{\text{Zeeman}} = \mu_B B\ g^{\text{eff}}\left(\vec{\Omega}\right)\ \hat{S}_z, \tag{17}$$

where effective Zeeman coupling is defined as

$$g^{\text{eff}}\left(\vec{\Omega}\right) = \sqrt{\vec{k}\ \overline{R^{(l)\to(m)}}\ \overline{R^{(m)\to(n)}}\ \underline{g}\quad \underline{g}\ R^{(m)\to(n)}\ R^{(l)\to(m)}\ \vec{k}}. \tag{18}$$

Note that the effective Zeeman coupling, $g^{\text{eff}}\left(\vec{\Omega}\right) = g^{\text{eff}}\left(\Theta,\Phi;\psi,\vartheta,\varphi\right)$, includes the "powder-like" membrane-normal orientation dependence {Θ, Φ} as well as the orientation dependence of fast changing rotational conformations defined with Euler angles $\{\psi,\ \vartheta,\ \varphi\}$. To take this into account while partial averaging due to fast rotational motion, we introduce

$$\underline{\tilde{G}}\left(\psi,\vartheta,\varphi\right) = \overline{R^{(m)\to(n)}}\ \underline{g}\ \underline{g}\ R^{(m)\to(n)}. \tag{19}$$

Similarly, we can transform the **hyperfine term** of Eq. (14):

$$\hat{H}_{\text{hyperfine}} = \overline{\left(\overline{R^{(lm)\to(l)}}\ \hat{\vec{I}} \right)}\ \overline{R^{(l)\to(m)}}\ \overline{R^{(m)\to(n)}}\ \underline{A}\ R^{(m)\to(n)}\ R^{(l)\to(m)}\ R^{(lm)\to(l)}\ \hat{\vec{S}}. \tag{20}$$

Using the transformation from/to the coordinate system of the local magnetic field. the hyperfine term can be rewritten as

$$\begin{aligned} \hat{H}_{\text{hyperfine}} &= \left(g^{\text{eff}}\left(\vec{\Omega}\right)\right)^2 \hat{\vec{I}}\, \overline{R^{(l)\to(m)}}\, \overline{R^{(m)\to(n)}}\, \underline{g}^{-1}\, \underline{A}\, \underline{g}^{-1}\ {}^{(m)\to(n)}\ R^{(l)\to(m)} \hat{\vec{S}} \\ &= \hat{\vec{I}}\ \underline{A}^{\text{eff}}\left(\vec{\Omega}\right)\ \hat{\vec{S}} \end{aligned}, \tag{21}$$

where the effective hyperfine coupling (tensor) is defined as

$$\underline{A}^{\text{eff}}\left(\vec{\Omega}\right)=\left(g^{\text{eff}}\left(\vec{\Omega}\right)\right)^{2}\ \overline{R^{(l)\to(m)}}\ \ \overline{R^{(m)\to(n)}}\ \underline{g}^{-1}\underline{A}\ \ \underline{g}^{-1}\ R^{(m)\to(n)}\ \ R^{(l)\to(m)}. \qquad (22)$$

Similarly to the effective Zeeman term, the effective hyperfine coupling, $\underline{A}^{\text{eff}}\left(\vec{\Omega}\right)=\underline{A}^{\text{eff}}\left(\Theta,\Phi;\psi,\vartheta,\varphi\right)$, includes the “powder-like” membrane-normal orientation dependence $\{\Theta, \Phi\}$ and the orientation dependence of fast changing rotational conformations defined with Euler angles $\{\psi, \vartheta, \varphi\}$. Note that both dependencies are involved also in the g^{eff} term, making the expression for A^{eff} even more complicated. In the same way as $\underline{\tilde{G}}$, we introduce

$$\underline{\tilde{A}}\left(\psi,\vartheta,\varphi\right)=\overline{R^{(m)\to(n)}}\ \ \underline{g}^{-1}\ \ \underline{A}\ \ \underline{g}^{-1}\ \ R^{(m)\to(n)}. \qquad (23)$$

Using the effective Zeeman and hyperfine term, the Hamiltonian can be written in the following compact form:

$$\hat{H}=\mu_B B\ \ g^{\text{eff}}\left(\vec{\Omega}\right)\ \hat{S}_z+\ \hat{\vec{I}}\ \ A^{\text{eff}}\left(\vec{\Omega}\right)\ \hat{\vec{S}}. \qquad (24)$$

Further simplification of the effective hyperfine term depends on the approximation one takes into account when solving the eigensystem equation. However, before solving the eigensystem equation, an important first step is taking into account, e.g., fast rotational motions in the membrane coordinate system, which implies partial averaging in the $\underline{\tilde{G}}\left(\psi,\vartheta,\varphi\right)$ and $\underline{\tilde{A}}\left(\psi,\vartheta,\varphi\right)$ terms.

2.3. Introducing Fast Motion of the Spin Probe

> When the spin probe wobbles, the effective Zeeman and hyperfine couplings change with orientation (they involve dependencies on $\{\Theta, \Phi\}$ as well as $\{\psi, \vartheta, \varphi\}$).

Suppose a wobbling spin probe in a membrane in a situation where the spin probe also is able to laterally diffuse. We already define that the wobbling — changing of $\{\psi, \vartheta, \varphi\}$ in time — is fast on the ESR timescale. On the other hand, the mean displacement of the spin probe molecule in the membrane is at largest a few lipid molecules per ESR timescale. Since the curvature of the membrane is usually not extremely high, we can say that the time variation of $\{\Theta, \Phi\}$ is much slower as compared to the time variation of $\{\psi, \vartheta, \varphi\}$ — actually we will assume $\{\Theta, \Phi\}$ to be constant on the ESR timescale. In such a case, the orientation dependence can be separated into two major contributions:

- Orientation of the molecule (or nitroxide group) relative to molecule average orientation in the membrane, that is, membrane normal ($\{\psi, \vartheta, \varphi\}$ dependences)

- Orientation of the local membrane normal relative to the external magnetic field ($\{\Theta, \Phi\}$ dependences)

However, sometimes the translational diffusion could be higher and the local curvature could be larger, such as in the case of membrane defects. In such cases one has to be careful in separating the two orientational dependencies.

> Fast rotational motion of a spin-labeled molecule on the ESR timescale averages the magnetic properties over all the possible orientations relative to the membrane normal.

Consequently, time averaging should be taken into account over the terms with $\{\psi, \vartheta, \varphi\}$ dependences in Eqs. (18) and (22). The $\underline{\tilde{G}}(\psi,\vartheta,\varphi)$ and $\underline{\tilde{A}}(\psi,\vartheta,\varphi)$ terms are transformed as follows:

$$\begin{aligned} \underline{\tilde{G}}(\psi,\vartheta,\varphi) \mapsto \underline{\tilde{G}}^{\text{avg}} &= \overline{\underline{\tilde{G}}(\psi(t),\vartheta(t),\varphi(t))}\,, \\ \underline{\tilde{A}}(\psi,\vartheta,\varphi) \mapsto \underline{\tilde{A}}^{\text{avg}} &= \overline{\underline{\tilde{A}}(\psi(t),\vartheta(t),\varphi(t))}\,. \end{aligned} \tag{25}$$

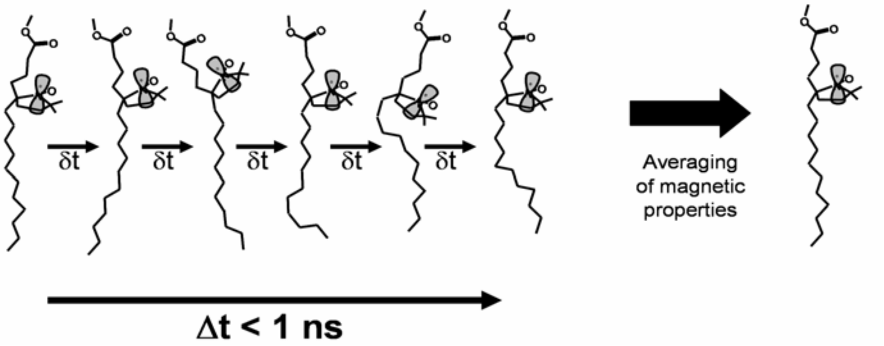

Figure 4. Averaging of the magnetic properties (Zeeman and hyperfine couplings).

The elements of $\underline{\tilde{G}}$ and $\underline{\tilde{A}}$ involve complicated expressions of trigonometric functions that should be averaged according to the motional restriction

$$\overline{f(\Omega)} = \int f(\Omega)\frac{dP}{d\Omega}d\Omega\,. \tag{26}$$

The definition intervals are [–π/2, π/2] for φ, [0, π/2] for ϑ, and [–π/2, π/2] for ψ, as indicated in Eq. (25). The full expressions for the averaged effective Zeeman coupling components and hyperfine coupling are given in Appendix 1 of this chapter (Eqs. (A.1)–(A.12)). Note that the terms involving sin(φ), cos(φ), sin(2φ), sin(ψ), cos(ψ), and sin(2ψ) vanish after averaging due to symmetry.

The averages in Eq. (25) can be determined in the following ways:

- Deduction from molecular dynamics simulations,
- Phenomenological expression with order parameters,
- Calculation from conformational probabilities, which can be derived from reorienting potentials.

The last two approaches are discussed in the following text.

> If probability functions are not directly known, the averages in Eq. (25) may be expressed in terms of **order parameters**.

$$\overline{\cos^2\left(\vartheta_{zz}\right)} = \overline{\cos^2\left(\vartheta\right)} = \frac{2S_z+1}{3}, \tag{27}$$

$$\overline{\cos^2\left(\vartheta_{zy}\right)} = \overline{\sin^2\left(\vartheta\right)}\ \overline{\sin^2\left(\varphi\right)} = \frac{2S_y+1}{3} = \frac{1}{3}\left(1-S_z\right)\left(1-\sigma\right)\ . \tag{28}$$

The most common order parameter, S_z, represents ordering along the long molecular axes in the case of a membrane spin label. The two extreme situations are: a completely isotropic case (a solution with no preferred orientation) and a completely ordered case. Note that S_z counts for an averaged projection of a tumbling molecule on its averaged direction. Typically, the value of S_z of a fatty acid spin probe in disordered phases of membranes is below 0.3, while it usually does not exceed 0.7 in the ordered phase.

The other order parameter, σ counts for the asymmetry/restrictions of the rotational motions around the long axes (averaged molecule position), with definition intervals being the same as for S_z. Partial averaging due to rotational motions around the long axes strongly depends on the size and conformational freedom of the spin-labeled molecule as well as the properties of the local environment — its sterical restrictions and dynamics. For example, the rotation of a spin-labeled lipid molecule around its long axes is more restricted than for a spin-labeled fatty acid molecule, resulting in higher σ. The same is true for a spin probe being close to rigid molecules like cholesterol. Note that σ rarely exceeds 0.7.

To be able to calculate all averages directly, one needs to know or define the probability functions.

In a **wobble or cone model**, the probability functions are defined as step functions:

$$\left\{\begin{matrix} 0<|\xi|<\xi_0 \Rightarrow \dfrac{dP}{d\xi} = \text{const} \\ \xi_0<|\xi|<\dfrac{\pi}{2} \Rightarrow \dfrac{dP}{d\xi} = 0 \end{matrix}\right\} \ \text{for}\ \ \xi = \{\psi, \vartheta, \varphi\}\ . \tag{29}$$

This leads to the following expressions:

$$\overline{\cos\left(\vartheta\right)^2} = \tfrac{1}{3}\left(\cos^2\left(\vartheta_0\right) + \cos\left(\vartheta_0\right) + 1\right), \tag{30}$$

$$\overline{\sin\left(\varphi\right)^2} = \frac{\varphi_0 - \frac{1}{2}\sin\left(2\varphi_0\right)}{2\varphi_0} = \frac{1}{2}\left(1 - \frac{\sin\left(2\varphi_0\right)}{2\varphi_0}\right), \tag{31}$$

$$\overline{\sin\left(\psi\right)^2} = \frac{\psi_0 - \frac{1}{2}\sin\left(2\psi_0\right)}{2\psi_0} = \frac{1}{2}\left(1 - \frac{\sin\left(2\psi_0\right)}{2\psi_0}\right), \tag{32}$$

$$\overline{\sin\left(2\vartheta\right)} = \tfrac{2}{3}\left(\cos\left(\vartheta_0\right) + 1\right)\sin\left(\vartheta_0\right), \tag{33}$$

$$\overline{\cos\left(\psi\right)} = \frac{\sin\left(\psi_0\right)}{\psi_0}. \tag{34}$$

Using appropriate probability functions, the averages can be expressed in terms of maximal wobbling angles. Note that in general one could have three maximal wobbling angles $\{\psi_0, \vartheta_0, \varphi_0\}$; however, two of them, ψ_0 and φ_0, are quite similar in this model. In fact, in the two limiting cases, close to no restrictions and close to complete restriction, ψ_0 and φ_0 are identical. Moreover, when ϑ_0 is small, ψ_0 and φ_0 are identical again. Therefore, we can often assume that ψ_0 is equal to φ_0. A second reason for using only one restriction parameter is purely numerical, since application of all three angles would make their determination ill-posed in an inverse-problem-solving case.

Alternatively, the probability function can be defined through a **Boltzmann distribution**:

$$\frac{dP}{d\Omega} = e^{-\frac{U(\Omega)}{kT}}, \tag{35}$$

and **reorienting potential** $U(\Omega)$ in generalized form of a Maier-Saupe potential:

$$U\left(\Omega\right) = U\left(\vartheta, \varphi\right) = A\ \cos^2\left(\vartheta\right) + \left(B + C\ \sin\left(\vartheta\right)^2\right)\cos^2\left(\varphi\right). \tag{36}$$

Using probability function Eq. (35) and reorienting the potential of Eq. (36), the averages of the trigonometric function can be calculated numerically in terms of potential constants A, B, and C. Below is only an example of how an average is calculated in a more general way:

$$\overline{\cos\left(\vartheta\right)^2} = \frac{\int \cos(\vartheta)^2 e^{\frac{A}{kT}\cos(\vartheta)^2 + \left(\frac{B}{kT} + \frac{C}{kT}\sin(\vartheta)^2\right)\cos(\varphi)^2} d\left(\cos(\vartheta)\right) d\varphi}{\int e^{\frac{A}{kT}\cos(\vartheta)^2 + \left(\frac{B}{kT} + \frac{C}{kT}\sin(\vartheta)^2\right)\cos(\varphi)^2} d\left(\cos(\vartheta)\right) d\varphi}. \tag{37}$$

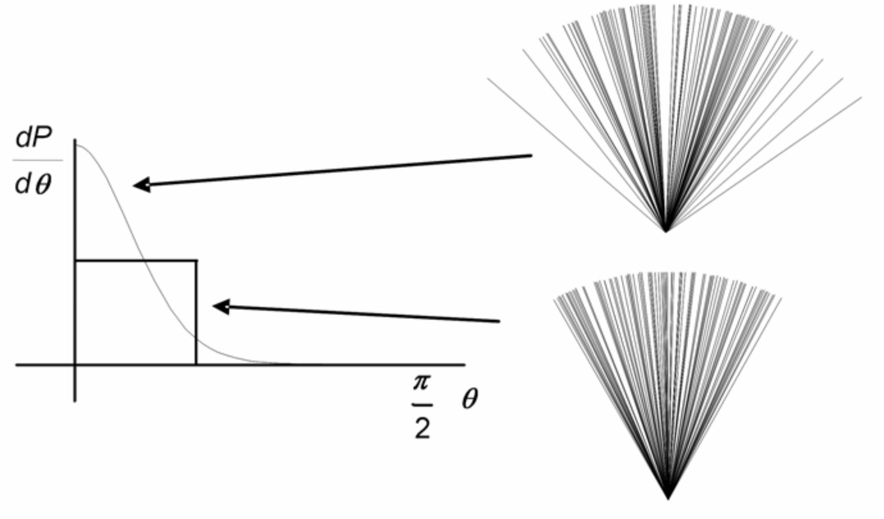

Figure 5. Schematic presentation of two different directional probability functions (on the left) and the corresponding distributions that yield the same $\cos(\vartheta)^2$ and consequently the same order parameter S_z; box-like distribution function and lower distribution pattern (lower right corner) correspond to the Cone (wobble) model, whereas the smooth distribution and the upper distribution pattern (upper right corner) correspond to a Boltzmann distribution with a simple symmetric Maier-Saupe reorienting potential (see (36)); for clarity, only one angle (ϑ) is presented.

2.4. Derivation of Resonant Fields

After motional averaging, the total spin Hamiltonian of Eq. (15) can be rewritten as

$$\begin{aligned}\hat{H} = \sum_i \Big[& \mu_B \vec{B}\ \overline{R_i^{(l)\to(m)}}\ \underline{\tilde{G}}^{\text{avg}}\ R_i^{(l)\to(m)}\ \hat{\vec{S}} \\ & + \Big|\vec{k}\ \overline{R_i^{(l)\to(m)}}\ \underline{\tilde{G}}^{\text{avg}}\ R_i^{(l)\to(m)}\ \vec{k}\Big|^2\ \hat{\vec{I}}\ \overline{R_i^{(l)\to(m)}}\ \underline{\tilde{A}}^{\text{avg}}\ R_i^{(l)\to(m)} \hat{\vec{S}} \Big] \qquad (38) \\ = \sum_i \Big[& \mu_B B\ g^{\text{eff}}(\Theta_i,\Phi_i)\ \hat{S}_z + \hat{\vec{I}}\ \underline{A}^{\text{eff}}(\Theta_i,\Phi_i)\ \hat{\vec{S}}\Big].\end{aligned}$$

Once again we want to stress that motional averaging cannot average out the orientation dependence of the local membrane normal relative to the magnetic field direction, unless lateral diffusion is high or membrane curvature is strong.

To find the eigenvalues of spin Hamiltonian Eq. (38), the all-spin operators in the hyperfine term should be expanded as shown for the electron spin operators in Eq. (11):

$$\begin{aligned}\hat{H}_i = {}&[\mu_B B\ \ g^{\mathrm{eff}}(\Theta_i,\Phi_i) + A_{zz}^{\mathrm{eff}}(\Theta_i,\Phi_i)\ \hat{I}_z \\ &+\overline{A_{xzyz}^{\mathrm{eff}}}(\Theta_i,\Phi_i)\ \hat{I}_+ + A_{xzyz}^{\mathrm{eff}}(\Theta_i,\Phi_i)\ \hat{I}_-]\hat{S}_z \\ &+\left[\overline{A_{xzyz}^{\mathrm{eff}}}(\Theta_i,\Phi_i)\ \hat{I}_z + \overline{A_{xyxy}^{\mathrm{eff}}}(\Theta_i,\Phi_i)\ \hat{I}_+ + A_{xxyy}^{\mathrm{eff}}(\Theta_i,\Phi_i)\ \hat{I}_-\right]\ \hat{S}_+ \\ &+\left[A_{xzyz}^{\mathrm{eff}}(\Theta_i,\Phi_i)\ \hat{I}_z + A_{xxyy}^{\mathrm{eff}}(\Theta_i,\Phi_i)\ \hat{I}_+ + A_{xyxy}^{\mathrm{eff}}(\Theta_i,\Phi_i)\ \hat{I}_-\right]\ \hat{S}_-\ .\end{aligned} \tag{39}$$

The full expressions for effective tensor couplings g^{eff}, $A_{zz}{}^{\mathrm{eff}}$, $A_{xzyz}{}^{\mathrm{eff}}$, $A_{xyxy}{}^{\mathrm{eff}}$, and $A_{xxyy}{}^{\mathrm{eff}}$ are given in Appendix A (Eqs. (A.13)–)A.17)). Note that the overbar in Eq. (39) indicates the complex conjugate of the corresponding quantities.

The **Hamiltonian matrix** (see §1 for an explanation) now becomes

$$\langle\hat{H}\rangle = \left(\begin{array}{cc|cc|cc} +\frac{1}{2}\left(G^{\mathrm{eff}}+A_{zz}^{\mathrm{eff}}\right) & \overline{A_{xzyz}^{\mathrm{eff}}} & +\frac{1}{2}\overline{A_{xzyz}^{\mathrm{eff}}} & \overline{A_{xyxy}^{\mathrm{eff}}} & 0 & 0 \\ A_{xzyz}^{eff} & -\frac{1}{2}\left(G^{eff}+A_{zz}^{eff}\right) & A_{xxyy}^{\mathrm{eff}} & -\frac{1}{2}\overline{A_{xzyz}^{\mathrm{eff}}} & 0 & 0 \\ \hline +\frac{1}{2}A_{xzyz}^{\mathrm{eff}} & A_{xxyy}^{\mathrm{eff}} & +\frac{1}{2}\left(G^{\mathrm{eff}}\right) & 0 & +\frac{1}{2}\overline{A_{xzyz}^{\mathrm{eff}}} & \overline{A_{xyxy}^{\mathrm{eff}}} \\ A_{xyxy}^{eff} & -\frac{1}{2}A_{xzyz}^{\mathrm{eff}} & 0 & -\frac{1}{2}\left(G^{\mathrm{eff}}\right) & A_{xxyy}^{\mathrm{eff}} & -\frac{1}{2}\overline{A_{xzyz}^{\mathrm{eff}}} \\ \hline 0 & 0 & +\frac{1}{2}A_{xzyz}^{\mathrm{eff}} & A_{xxyy}^{\mathrm{eff}} & +\frac{1}{2}\left(g^{\mathrm{eff}}-A_{zz}^{\mathrm{eff}}\right) & -\overline{A_{xzyz}^{\mathrm{eff}}} \\ 0 & 0 & A_{xyxy}^{eff} & -\frac{1}{2}A_{xzyz}^{eff} & -A_{xzyz}^{\mathrm{eff}} & -\frac{1}{2}\left(g^{\mathrm{eff}}-A_{zz}^{\mathrm{eff}}\right) \end{array}\right), \tag{40}$$

where G^{eff} corresponds to $\mu_B{\cdot}B{\cdot}g^{\mathrm{eff}}$.

The Hamiltonian matrix is a block-tridiagonal Hermitian (self-adjoint) matrix. Although the Hamiltonian matrix has complex elements, please note that it is a Hermitian matrix and therefore has real eigenvalues.

In general the matrix of Eq. (40) cannot be solved analytically. Although there are some efficient numerical methods to find the eigenvalues of Eq. (40), some approximations can be made without reducing the accuracy significantly. The matrix below shows the order of magnitudes of the individual matrix elements in field units of mT for in the case of X-band ESR:

$$\underline{E} = \langle\hat{H}\rangle = \left(\begin{array}{cc|cc|cc} 101 & 1-i & 1-i & 1-0.1i & 0 & 0 \\ 1+i & -101 & 1 & -1+i & 0 & 0 \\ \hline 1+i & 1 & 100 & 0 & 1-i & 1-0.1i \\ 1+0.1i & -1-i & 0 & -100 & 1 & -1+i \\ \hline 0 & 0 & 1+i & 1 & 99 & -1+i \\ 0 & 0 & 1+0.1i & -1-i & -1-i & -99 \end{array}\right). \tag{41}$$

Note that in Eq. (41) i is the imaginary unit. The exact solution of the matrix above would give us the following eigenvalues:

$$\{E_i\} = \{102.26,\ -102.25,\ 100.02,\ -100.01,\ 97.77,\ -97.77\}. \tag{42}$$

By neglecting different non-diagonal terms, the solutions can be found also analytically; however different approximations yield solutions with different relative accuracy:

S_z I_z terms only (relative accuracy 1%, absolute accuracy 1 mT)

$$\{E_i\} = \{101,\ -101,\ 100,\ -100,\ 99,\ -99\} \tag{43}$$

(S_z, S_+, S_-) I_z terms only (relative accuracy 1%, absolute accuracy 1 mT)

$$\{E_i\} = \{101.01,\ -101.01,\ 100,\ -100,\ 99.01,\ -99.01\} \tag{44}$$

S_z (I_z, I_+, I_-) terms only (relative accuracy 0.01%, absolute accuracy 0.01 mT)

$$\{E_i\} = \{102.24,\ -102.24,\ 100,\ -100,\ 97.76,\ -97.76\} \tag{45}$$

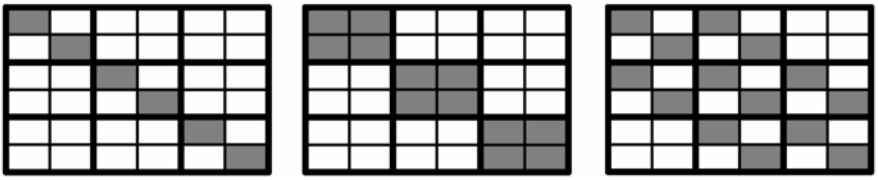

Figure 6. Schematic presentation of different approximations to Hamiltonian matrices: "S_z I_z terms only" (left), "(S_z, S_+, S_-)I_z terms only" (center), "S_z (I_z, I_+, I_-) terms only" (right).

> Among the solutions that can be found analytically, the highest accuracy is achieved by including the diagonals of the super-block-diagonal and sub-block diagonal.

For the approximation "*S_z (I_z, I_+, I_-) terms only*" the following general expressions for the eigenvalues can be derived:

$$E_{\left|\pm\frac{1}{2},M_I\right\rangle} = \pm\frac{1}{2}\left(\mu_B B\ g^{\text{eff}}(\Theta_i,\Phi_i) + M_I\sqrt{\left(A_{zz}^{\text{eff}}(\Theta_i,\Phi_i)\right)^2 + 2\left|A_{xzyz}^{\text{eff}}(\Theta_i,\Phi_i)\right|^2}\right), \tag{46}$$

yielding the energies of the ESR transitions:

$$\Delta E_{M_I} = \mu_B B\ g^{\text{eff}}(\Theta_i,\Phi_i) + M_I\sqrt{\left(A_{zz}^{\text{eff}}(\Theta_i,\Phi_i)\right)^2 + 2\left|A_{xzyz}^{\text{eff}}(\Theta_i,\Phi_i)\right|^2}\ . \tag{47}$$

Finally, the resonant fields are calculated from resonant equation

$$\Delta E_{M_I} = h\nu \rightarrow B = \frac{h\nu - M_I\sqrt{\left(A_{zz}^{\text{eff}}(\Theta_i,\Phi_i)\right)^2 + 2\left|A_{xzyz}^{\text{eff}}(\Theta_i,\Phi_i)\right|^2}}{\mu_B\ g^{\text{eff}}(\Theta_i,\Phi_i)}\ . \tag{48}$$

Note that the typical absolute error of a resonant field value of about 0.01 mT for X-band ESR in this approximation is much less than the typical linewidths of a nitroxide spin probe. An accurate spectral simulation tool can therefore apply up to 100 points-per-mT sweep without inducing spectral distortions.

In case of higher ESR frequencies, the absolute error decreases almost linearly with frequency and the relative error almost quadratically.

Note that when one replaces ^{14}N for ^{15}N, which has a nuclear spin of ½, the resonant frequencies can be calculated more directly. In this case the Hamiltonian matrix looks like

$$\left\langle \hat{H} \right\rangle = \left(\begin{array}{cc|cc} +\frac{1}{2}\left(G^{\mathrm{eff}} + \frac{1}{2}A_{zz}^{\mathrm{eff}}\right) & \frac{1}{2}\overline{A_{xzyz}^{\mathrm{eff}}} & +\frac{1}{2}\overline{A_{xzyz}^{\mathrm{eff}}} & \overline{A_{xyxy}^{\mathrm{eff}}} \\ \frac{1}{2}A_{xzyz}^{\mathrm{eff}} & -\frac{1}{2}\left(G^{\mathrm{eff}} + \frac{1}{2}A_{zz}^{\mathrm{eff}}\right) & A_{xxyy}^{\mathrm{eff}} & -\frac{1}{2}\overline{A_{xzyz}^{\mathrm{eff}}} \\ \hline +\frac{1}{2}A_{xzyz}^{\mathrm{eff}} & A_{xxyy}^{\mathrm{eff}} & +\frac{1}{2}\left(g^{\mathrm{eff}} - \frac{1}{2}A_{zz}^{\mathrm{eff}}\right) & -\frac{1}{2}\overline{A_{xzyz}^{\mathrm{eff}}} \\ A_{xyxy}^{\mathrm{eff}} & -\frac{1}{2}A_{xzyz}^{\mathrm{eff}} & -\frac{1}{2}A_{xzyz}^{\mathrm{eff}} & -\frac{1}{2}\left(g^{\mathrm{eff}} - \frac{1}{2}A_{zz}^{\mathrm{eff}}\right) \end{array} \right), \qquad (49)$$

where G^{eff} corresponds to $\mu_B \cdot B \cdot g^{\mathrm{eff}}$. In the approximation "*S_z (I_z, I_+, I_-) terms only*" the above expression can be transformed to

$$\left\langle \hat{H} \right\rangle = \left(\begin{array}{cc|cc} +\frac{1}{2}\left(G^{\mathrm{eff}} + \frac{1}{2}A_{zz}^{\mathrm{eff}}\right) & 0 & +\frac{1}{2}\overline{A_{xzyz}^{\mathrm{eff}}} & 0 \\ 0 & -\frac{1}{2}\left(G^{\mathrm{eff}} + \frac{1}{2}A_{zz}^{\mathrm{eff}}\right) & 0 & -\frac{1}{2}\overline{A_{xzyz}^{\mathrm{eff}}} \\ \hline +\frac{1}{2}A_{xzyz}^{\mathrm{eff}} & 0 & +\frac{1}{2}\left(g^{\mathrm{eff}} - \frac{1}{2}A_{zz}^{\mathrm{eff}}\right) & 0 \\ 0 & -\frac{1}{2}A_{xzyz}^{\mathrm{eff}} & 0 & -\frac{1}{2}\left(g^{\mathrm{eff}} - \frac{1}{2}A_{zz}^{\mathrm{eff}}\right) \end{array} \right), \qquad (50)$$

which can be solved analytically. After solving the eigensystem, a general expression for resonant fields becomes

$$\Delta E_{M_I} = h\nu \to B = \frac{h\nu - M_I \sqrt{\left(A_{zz}^{\mathrm{eff}}\left(\Theta_i, \Phi_i\right)\right)^2 + 4\left|A_{xzyz}^{\mathrm{eff}}\left(\Theta_i, \Phi_i\right)\right|^2}}{\mu_B \;\; g^{\mathrm{eff}}\left(\Theta_i, \Phi_i\right)}. \qquad (51)$$

3. STRATEGIES FOR CALCULATING POWDER SPECTRA

3.1. From Resonant Fields Values to Stick Spectra

A simple ESR spectrum of a nitroxide spin probe with a particular orientation is represented by a Lorentzian-shaped triplet, actually acquired in its first-derivative form due to field modulation.

$$\overline{P}(B) \propto \frac{1}{1 + \left(\dfrac{B - B_r(M_I)}{\Delta B(M_I)}\right)^2} \xrightarrow{\text{Modulation}} \frac{d\overline{P}(B)}{dB} \propto \frac{\left(B_r(M_I) - B\right)}{\left(1 + \left(\dfrac{B - B_r(M_I)}{\Delta B(M_I)}\right)^2\right)^2}. \qquad (52)$$

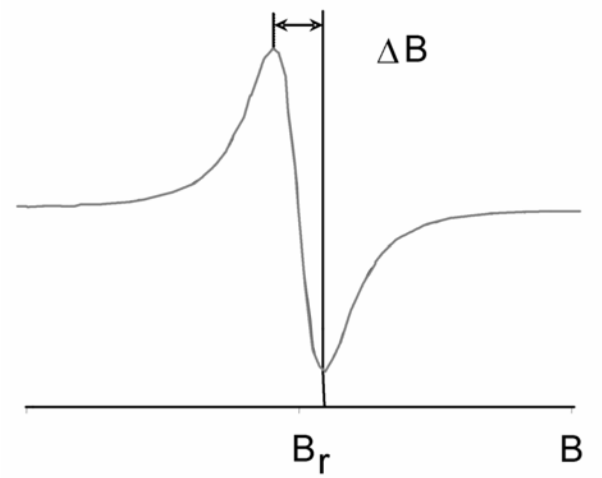

Figure 7. Typical ESR lineshape: — derivative of a Lorentzian function.

The resonant-field positions $B_r(M_I)$ are calculated according to resonance equation Eq. (48) at the corresponding orientation. Linewidths $\Delta B(M_I)$ are determined by a linewidth model, for example, by the Redfield theory in the case of a fast motion approximation.

The Lorentzian lineshape arises from the exponential decay of the magnetization in a rotating frame of reference.

At physiological temperatures and non-saturating ESR conditions, spin dephasing (decay of coherent magnetization) represents the most common relaxation mechanisms due to the motion of spin probe molecules.

Since a common spin-labeled sample involves many spin probe molecules oriented in different directions, the ESR spectrum should be calculated as a convolution of the resonant field distribution $d\rho/dB_r$, taking into account the Lorentzian lineshape for all triplet lines:

$$\frac{d\overline{P}(B)}{dB}(M_I) \propto \int_{B_r} \frac{d\rho(B_r(M_I))}{dB_r} \, \frac{d\overline{P}(B;B_r(M_I))}{dB} dB_r \,. \tag{53}$$

Calculation of the convolution in Eq. (53) represents the most time-consuming step in the calculation procedure for ESR spectra. Therefore, a lot of effort is required to reduce its numerical cost in any implementation algorithm.

Every such convolution calculation costs around 1 MFLO, or around a millisecond on 1-GFLOPS processor.

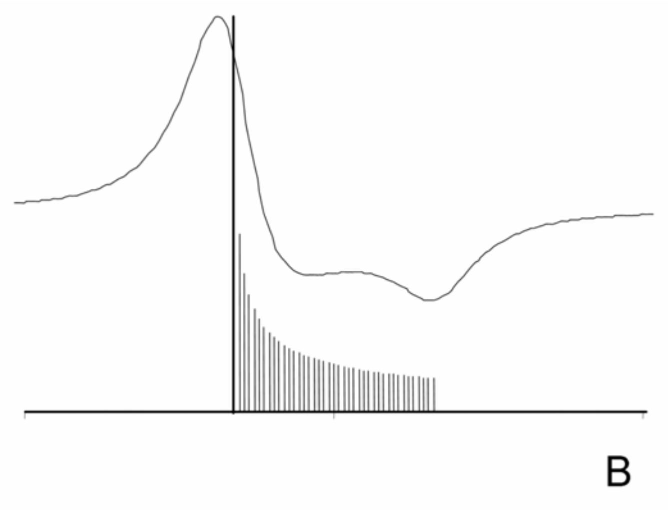

Figure 8. Typical numerical convolution in an ESR lineshape calculation: the resonant field probability function (histogram-like "stick spectra"), which is convoluted with the Lorentzian lineshape from Figure 6, is represented together with the resulting spectral lineshape.

3.2. Summation Schemes and Resolution: Reducing the Computation Time

> Generally, the convolution integral (or sum) can be done with a **Fast Fourier Transform algorithm** (FFT) or **direct summation scheme**.

To choose a fast algorithm consider the following points:

- The costs of direct convolution and the FFT algorithm increase with spectral size N like N^2 and $N \cdot \mathrm{Log}_2(N)$, respectively, making the FFT algorithm more efficient than a direct scheme in convoluting large spectra (several thousands points);
- "Zero" intervals of a resonant field distribution with known resonant field extremes enable a significant acceleration of the direct scheme, making it more efficient than FFT in convoluting small spectra (up to thousand points);
- To avoid FFT wiggles on the spectral wings, zero padding or equivalent approaches are needed, giving rise to additional costs.

According to the maximal hyperfine splitting of 7 mT in the case of a nitroxide and resolution requirements of around 0.01 mT, the spectral size can be reduced to 1024 calculated points. For this case an accelerated direct scheme can be more efficient and accurate than an FFT scheme. However, for higher-resolution requirements and related higher spectral sizes, FFT will become more efficient at the same accuracy.

3.3. Matching Resolution and Accuracy

Before performing a convolution integral (or sum), resonant field distribution $d\rho/dB_r$ has to be constructed for all three resonant lines. Remember that this distribution results in different motional-averaged orientations of the spin probe molecules, which actually represent the orientation distribution of the membrane normal vector $d\rho/d\Omega$:

$$\frac{d\rho(B_r(M_I))}{dB_r} = \frac{d\rho(\Omega)}{d\Omega}\frac{d\Omega(\Omega;M_I)}{dB_r}. \tag{54}$$

The orientation distribution is basically described by the geometry of the spin-labeled sample taking into account the dynamic and static properties on the partitioning as well.

Note that differential $d\Omega = \sin(\Theta)\, d\Theta\, d\Phi$ also contains the phase space volume.

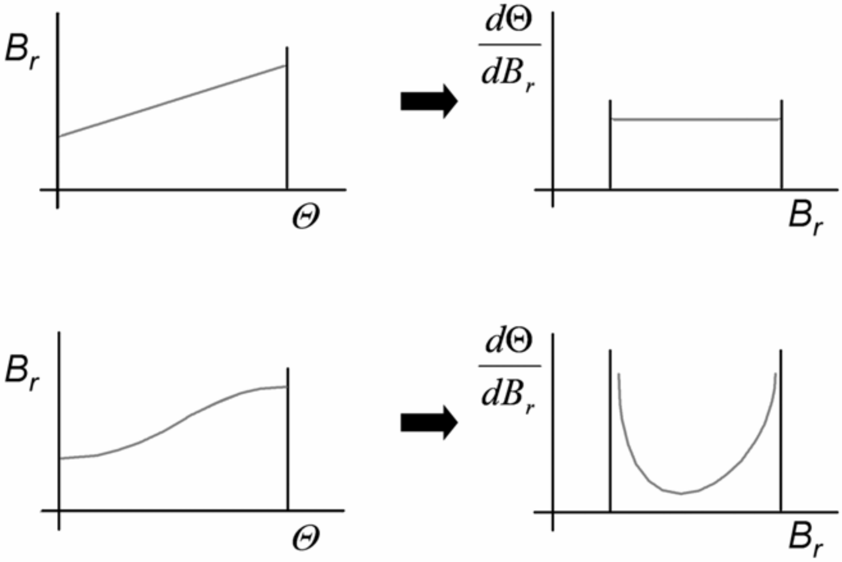

Figure 9. Linear (top) and realistic (bottom) resonant field dependences on the direction and the corresponding derivatives that are defined in Eq. (53) and used in Eq. (54).

Construction of the resonant field distribution involves summation over different directions. To reduce the time cost, the size of this summation ensemble should be optimized according to the resolution requirements and anisotropy of the effective magnetic properties (see Table 3).

The resolution should be equal to the magnetic-field-sweep-step-per-point (which indirectly depends on the linewidths), whereas the anisotropy of the magnetic field properties is determined as the maximal interval of the resonant fields among all three orthogonal directions and all three lines.

Table 3. Resolution Requirements and Anisotropy of the Effective Magnetic Properties

No. of points per sweep	**Resolution requirement**	S_z ordering	σ ordering	Maximal resonant field intervals
$\Delta N/\Delta B$ [points/mT]	**δB [mT]**	S_z [..]	σ [..]	$\Delta B_{\mathrm{r,Mi}} \rightarrow \mathbf{Max}(\Delta \boldsymbol{B}_{\mathbf{r}})$ **[mT]**
100	**0.01**	0.2	0	0.4, 0.2, 0.7 → **0.7**
100	**0.01**	0.5	0	1.0, 0.4, 1.8 → **1.8**
100	**0.01**	0.5	1	1.8, 1.0, 2.0 → **2.0**
100	**0.01**	0.8	1	2.1, 1.1, 3.2 → **3.2**

In the last example from Table 3 one needs to calculate the resonant field interval of 3.2 mT with a resolution of 0.01 mT. In this case at least, 320 spin probes should be arranged in different directions to cover one quarter of a (phase space) sphere to match the resolution requirement. If the resonant field would change linearly with direction (see Figure 9, top), a linear grid of 400 directions would be sufficient to produce a smooth resonant field distribution. However, this dependence is far from being linear (see Eq. (54) and Figures 9 and 10). To satisfy the resolution requirement everywhere on the resonant field interval and accurately construct a smooth (and correct) resonant field distribution; the number of points should be increased by one order of magnitude.

In order not to exceed the accuracy of the resonant field far beyond the resolution limit and simultaneous dramatically increase the time cost, a two-dimensional linear interpolation of resonant fields can be applied. The simplest two-dimensional linear interpolation grid of 400 can be extended nine times with only a twofold increase in time cost at the same accuracy relative to the resonant field grid used in the convolution summation.

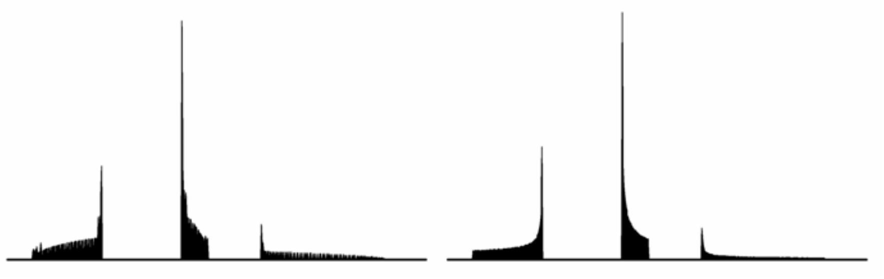

Figure 10. Non-smooth (left) and smooth (right) distributions as a result of rough and fine meshes and highly nonlinear resonant field dependences on the direction (from Figure 9).

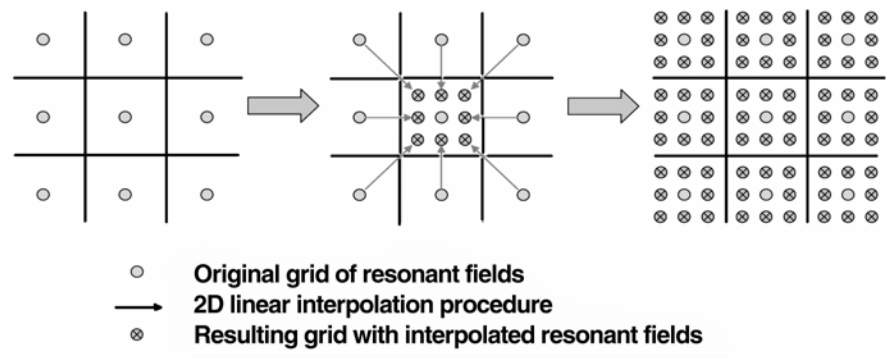

Figure 11. Schematic presentation of a grid expansion by a 2D linear interpolation.

3.4. Implementing Different Geometries and Directors Distributions

The most straightforward calculation of the resonant field distribution implies simple summation over the azimuthal and elevation angles (see Figure 12). In this general notation, any geometry can be implemented within $d\rho/d\Omega$ of Eq. (54).

In many cases, simple summation over the azimuthal and elevation angle leads to a highly non-smooth distribution of directions, resulting in a non-optimized summation scheme (see Figure 9).

In the isotropic case ($d\rho/d\Omega = 1$), many calculation steps are used to cover a small part of a phase space when the elevation angle and volume of the phase space approach zero (see Figure 12). Therefore, other summation schemes should be used to minimize time cost.

An efficient summation scheme is usually derived with the strategy of equalizing the phase space volume.

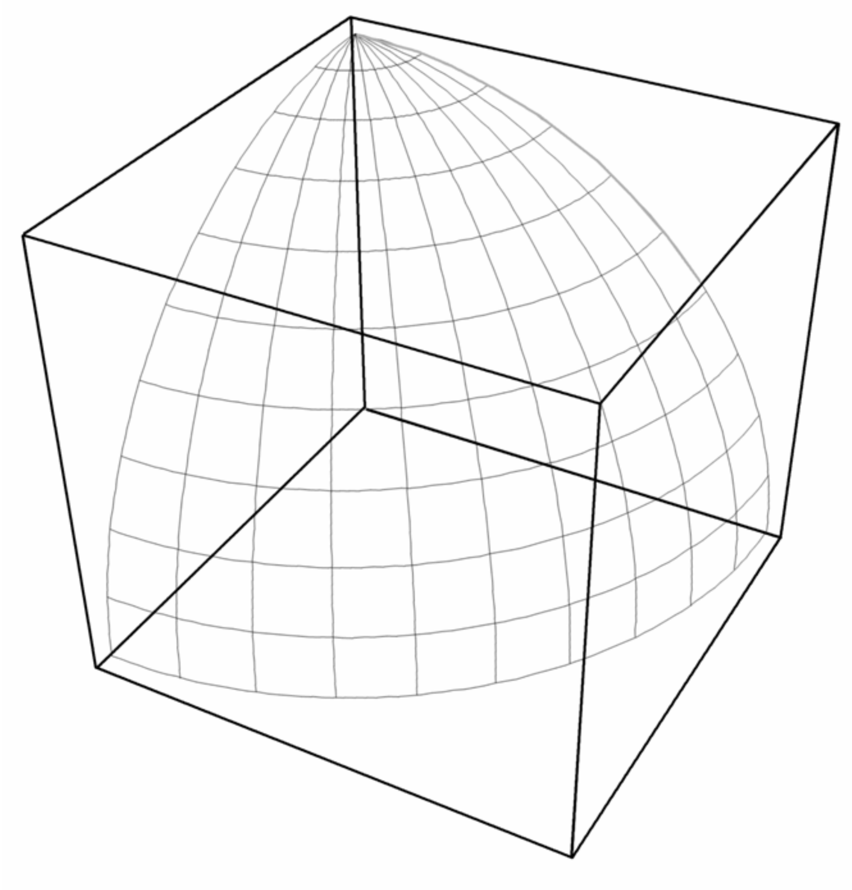

Figure 12. General and simple summation over azimuthal and elevation angles.

One of the most simple and also quite efficient summation schemes involves reduction of the azimuthal grid proportional to the elevation angle (see Figure 13).

Splitting the spherical surface into an ordered mesh of triangles could also be an efficient summation scheme. A typical example is the application of a geodesate, icosahedron, or dodecahedron (meshed projection of a icosahedron or dodecahedron onto a sphere; see Figure 14).

A simple experimental system that can be covered by an “isotropic” model is a model membrane dispersion (dispersion of liposomes in a buffer). Also dispersion of biological cells with other-than-spherical shape can be covered by this model, if the cells do not stack and are equally oriented in all directions.

Other geometries can be implemented by introducing directional probability $d\rho/d\Omega$ into Eq. (54).

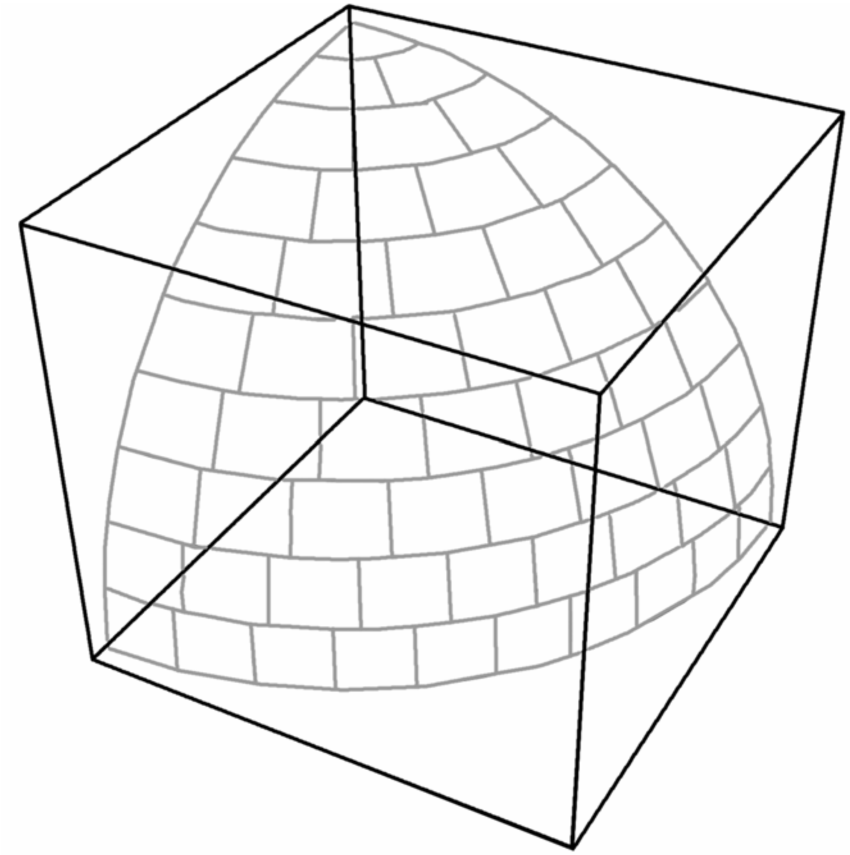

Figure 13. Efficient summation scheme: summation with reduction of azimuthal grid proportional to the elevation angle.

The directional probability can be defined in different ways, through a geometry consideration or a statistical probability distribution. In case of an oriented membrane, for example, one can define the directional probability with a reorienting potential (Maier-Saupe form) and a Boltzmann distribution function:

$$\frac{d\rho}{d\Theta} \tilde{\propto} e^{-\frac{U}{kT}} = e^{\frac{A}{kT}\cos^2(\Theta)}. \tag{55}$$

Since an efficient summation scheme depends on the geometry, any summation scheme should be optimized independently (of the "isotropic" case) to achieve reliable results, fastest computation times and accurate simulated spectra. For example, a summation scheme with a reduction of the azimuthal grid proportional to

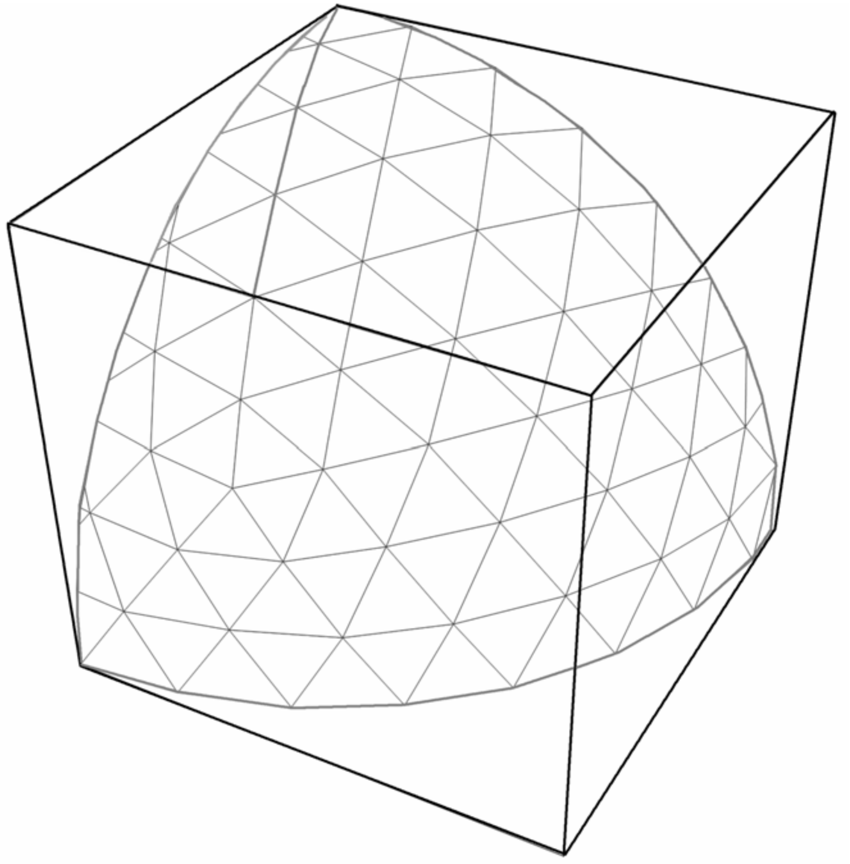

Figure 14. Another example of efficient summation schemes: summation over the geodesate of the icosahedron.

the elevation angle that is optimized for the isotropic case can be quite inadequate in the case of oriented membranes. This is especially true if the orientation of the membrane director is close to $\Theta = 0$. In this case the directional distribution vanishes close to the $\Theta = \pi/2$, where the “volume factor” is maximal.

In the case of oriented membranes, an efficient summation scheme could again be derived with the strategy of equalizing the phase space volumes. Due to the very low orientation probabilities at directions perpendicular to the membrane (acyl chains cannot be oriented in the membrane plane), we can modify the summation scheme from Figure 13 by reducing the grid of elevation angles near $\Theta = \pi/2$ (see Figure 15).

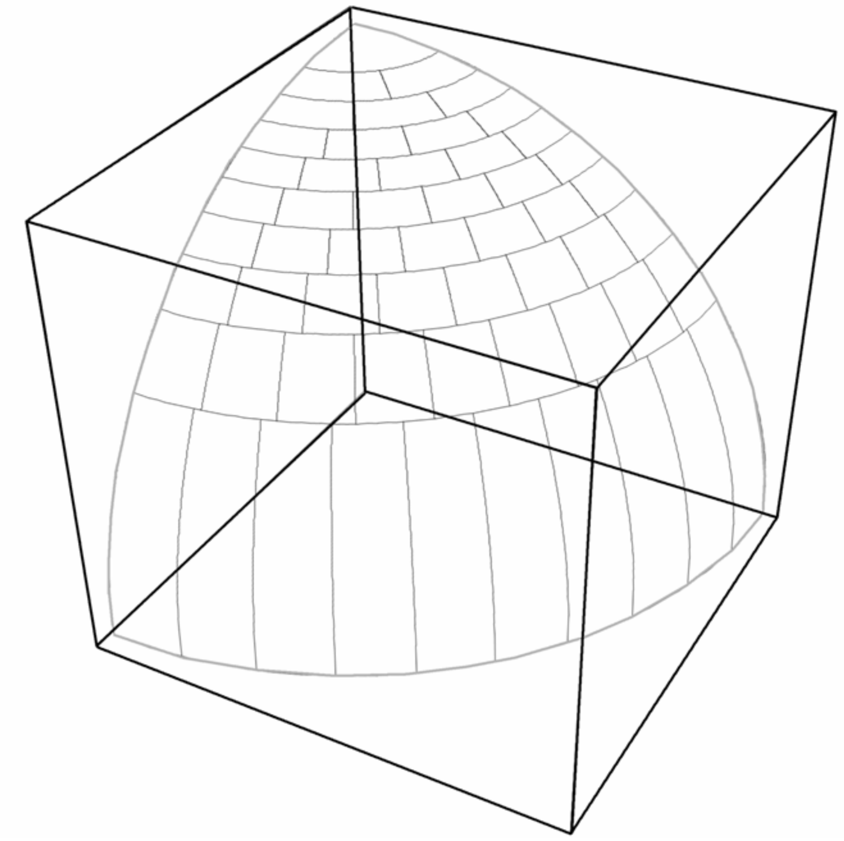

Figure 15. More efficient summation schemes for oriented membranes.

Using the above principles, optimization of summation schemes can be done automatically, making the simulation models more robust and fast at the same time.

In case of various membrane defects like pores and necks, one can define a directional probability using a modified phase space volume.

A pore or neck is a point-like defect type that can occur in a membrane stack. A pore actually represents a point where two monolayers of the same bilayer come close to each other. The whole structure possesses an inverse cylindrical symmetry with the lipid headgroup oriented to the symmetry axis of the structure (see Figure 16, left). Necks are points where two monolayers of the neighboring bilayers are close to each other. The whole structure possesses a cylindrical symmetry with the lipid headgroup oriented outward the symmetry axis of the structure (see Figure 16, right). Both structures possess a cylindrical symmetry, so there is no φ dependence in the orientational distribution. Since the phase space volume (of the isotropic distribution) sin(Θ) can be thought of as part of a spherical area, *dS*, defined within a constant Φ and Θ grid, one can define a similar expression for the pore/neck geometry by $dS \propto 1 - \gamma \sin(\Theta)$, where γ represents the ratio between bilayer thickness *d* and pore outer diameter *D*. The definition interval for γ is [0,1]. Close-to-zero values correspond to extremely large holes in pores, whereas close-to-one values correspond to pores without holes. The same expression is valid also for neck-type defects by taking γ = ½.

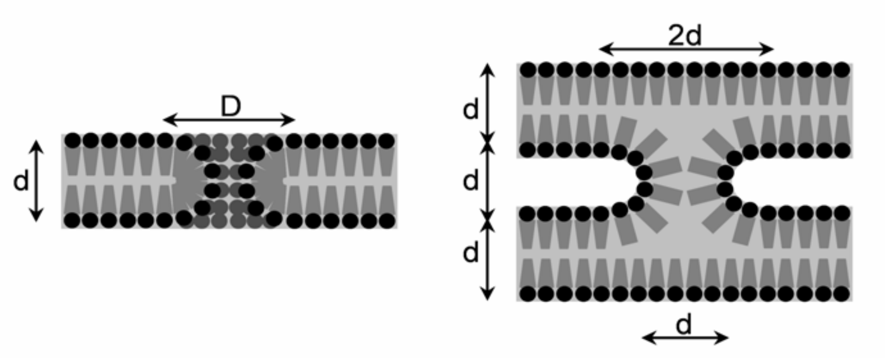

Figure 16. Pore and neck geometry: cross-section of the pore (left) and neck (right).

3.5. Implementing the Transition Probability Correction Factor

ESR transitions are induced by an oscillating microwave magnetic field, perpendicular to the static magnetic field. Using the "Fermi golden rule of quantum mechanics," the transition probability between the two spin states +½ and –½ can be expressed by the off-diagonal element of the Hamiltonian matrix:

$$w \propto \left| \left\langle +\tfrac{1}{2}, M_I \right| \hat{H}_{\text{microwave}} \left| -\tfrac{1}{2}, M_I \right\rangle \right|^2 , \tag{56}$$

where the microwave-field interaction term can be written in the form of a Zeeman term:

$$\hat{H}_{\text{microwave}} = \mu_B \vec{B}_{\text{microwave}} \, \underline{g} \, \hat{\vec{S}} . \tag{57}$$

Taking into account proper coordinate systems where the quantities in the above equation are well defined as well as the proper direction of the microwave magnetic field ($^{(l)}x$-axis), the Zeeman term becomes

$$\hat{H}_{\text{microwave}} = \mu_B B_{\text{microwave}} \, {}^{(l)}\vec{i} \; \overline{R^{(l)\to(m)}} \; \overline{R^{(m)\to(n)}} \; \underline{g} \; R^{(m)\to(n)} \; R^{(l)\to(m)} \; R^{(lm)\to(l)} \; \hat{\vec{S}} . \tag{58}$$

Introducing the definitions in Eqs. (5), (6), and (11) and the motional averaged effective Zeeman coupling g^{eff} from Eq. (18), Eq. (63) can be written in a more compact form as

$$\hat{H}_{\text{microwave}} = \mu_B B_{\text{microwave}} \; g^{\mathrm{eff}}(\Theta,\Phi) \; \tfrac{1}{2}\left(\hat{S}^{+} + \hat{S}^{-}\right). \tag{59}$$

The transition probability equation therefore transforms into

$$w \propto \left(g^{\mathrm{eff}}(\Theta,\Phi)\right)^2 \; \left|\left\langle +\tfrac{1}{2}, M_I \right| \tfrac{1}{2}\left(\hat{S}^{+} + \hat{S}^{-}\right) \left| -\tfrac{1}{2}, M_I \right\rangle\right|^2 \propto \left(\tfrac{1}{2} g^{\mathrm{eff}}(\Theta,\Phi)\right)^2. \tag{60}$$

In numerical algorithms one can use the following “unit-free” correction factor instead:

$$w \propto \left(\frac{g^{\mathrm{eff}}(\Theta,\Phi)}{g_0}\right)^2 . \tag{61}$$

Note that the relative effect of this correction is only about 0.8%, which corresponds to an error that is easily introduced by model averaging, summation schemes, and convolution integrals. Therefore, the transition probability correction is rarely needed in nitroxide spectra simulation.

4. SOLVING AN INVERSE PROBLEM AND CONDENSATION OF RESULTS

4.1. Phase Space of the Problem: Parameterization

To characterize a system by means of any experimental approach, one should understand the value of the experimental response function and its dependence on various boundary (stress) conditions. In case of ESR spectroscopy, one should therefore be able to simulate the changes in the spectral lineshape due to interactions within the system and due to interaction with external fields.

> Any simulation involves parameterization of the system, i.e., a set of parameters that defines the response function — the ESR spectra in case of ESR spectroscopy.

Some of the parameters (let us denote them *group 0 constants*) involved in a spectral simulation model do not define the exploring system, but are connected directly to the measuring conditions. In the case of ESR spectroscopy these constant parameters are:

- ESR band properties such as microwave power, frequency, and center field

- Scan properties: field sweep interval and scan speed
- RC filtering parameters including modulation conditions
- Magnetic properties of paramagnetic molecules in a reference environment (tensors).

A second group of parameters that affects the response function (denoted *group A parameters*) defines the properties of the system. In the case of ESR spectroscopy these are:

- Motional averaging parameters that measures the anisotropy of motion (e.g., order parameters)
- Motional rate parameters (e.g., rotation correlation times)
- Environmental corrections to magnetic properties (e.g., polarity correction factors)
- Parameters that measure inter-paramagnetic interactions (e.g., spin–spin exchange between molecules of the same or different species)

In addition to the parameters above, any complex-system modeling should define

- Heterogeneity of the system
- Distribution properties (of the paramagnetic species) between different compartments

These parameters are easily introduced by expansion of the basic set of *group A* parameters. Any compartment (domain, aggregate, phase, etc.) therefore possesses a unique set of *group A* parameters in addition to a *proportion* that defines the amount of nitroxide spin probe molecule in this particular compartment. Complex modeling can also involve the definition of the distribution functions as well as the dynamical properties of the system on the system scale (possible rearrangements, non-equilibrium transport, fast exchange between compartments, etc.).

> To provide a more reliable characterization of a complex system, more different spectroscopic and other experiments have to be applied.

4.2. Solving an Inverse Problem

The experimental response of ESR defined by the *group 0 constants* is used to determine the *group A parameters* of a certain biological system. When characterizing a complex biological system, only efficient modeling and a comparison of the experimental and modeled response function enable extraction of biosystem parameters. Resolving the *group A parameters* via system response modeling is usually called **inverse problem solving** (see Figure 17). However, inverse problem solving strongly depends on the complexity of the phase space, which (in a single experiment) relates to the number of *group A* parameters.

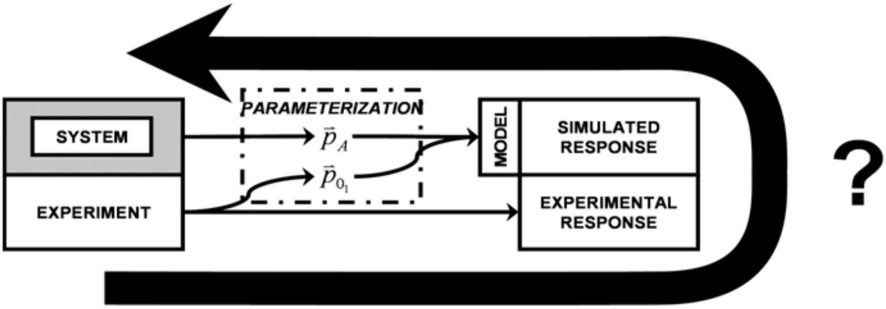

Figure 17. Inverse problem solving.

The simplest model for the ESR spectral shape simulations involves at least $N_A \geq 4$ spectral parameters (*group A*), whereas the response of a more complex system with m compartments can be defined with at least $m \cdot (N_A + 1) - 1$ parameters.

Note that the complexity of the phase space can increase significantly. When modeling the response of a complex system also the resolution limit of ESR should be considered. This is the maximum number of spectral parameters that can be extracted from a single ESR experiment and turns out to be about 30. This number depends on the ESR linewidths and maximal magnetic field anisotropy. Note also that some pairs of parameters can be partially (anti-)correlated, making determination of the parameters even more complicated.

Solving the inverse problem can be a non-trivial task, to be performed successfully.

A typical membrane simulation model can involve, for example, 3 domains with 5 + 1 parameters per domain, resulting in 17 parameters that should be determined from the ESR spectra to characterize the biosystem. To define each of the 17 parameters with an average error of only 10% (10 points per axis), this would result in a phase space volume of 10^{17} points. If each spectrum costs at least 1 ms of calculation time, it would take around 10^6 years to scan the whole phase space.

The enormous size of an ordinary phase space that is involved in modeling of the response function of a complex system calls for robust optimization methods that can be applied to solve the inverse problem. Simple phase space scans will not be efficient at all.

4.3. Characterization Process and Possible Ways of Solving the Inverse Problem

In a typical characterization, the experimentally measured response function has to be compared with a simulated one defined with a set of *group 0* constants and a set of *group A* parameters.

The main task of the characterization procedure is to vary a set of *group A parameters* to find the best match of the corresponding spectral lineshape to the experimentally measured spectral lineshape.

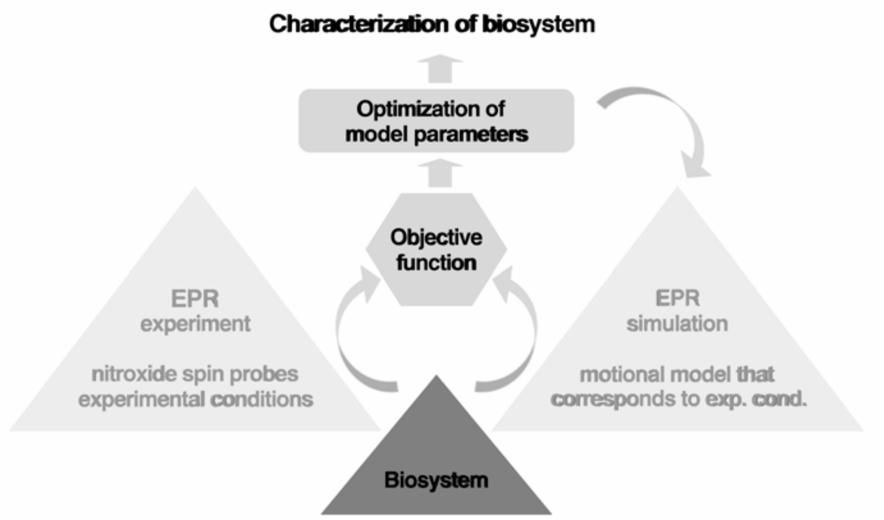

Figure 18. Characterization of a biosystem with ESR spectral simulation in a motional averaging model.

To efficiently navigate the optimization procedure, a fitness function is introduced. It measures the goodness of fit of the simulated spectrum with the experimental one. Most frequently, the measure is chosen to be the reduced χ^2, i.e., the sum of the squared residuals between the experimental and simulated spectra divided by the squared standard deviation of the experimental points σ, and by the number of points in the experimental spectrum N:

$$\chi^2 = \frac{1}{N}\sum_{j=1}^{N}\frac{(y_j^{\mathrm{exp}} - y_j^{\mathrm{sim}})^2}{\sigma^2}. \tag{62}$$

Standard deviation σ is assessed numerically from points in the simulated spectrum regions where the derivatives are close to zero, usually at both ends of the spectrum. Several other fitness functions can be selected as well (like island-weighted χ^2, correlation length functions, maximal difference functions, difference at constant positions, etc.). The convergence of the optimization method can depend on the applied objective function especially due to a different sensitivity to broad lines. In general some numerical transformations may be needed before an objective function can be applied.

In addition, convergence of the optimization routine is affected also by a set of “internal” optimization constants — *group B constants*, which define the scalable properties of the optimization routine. These constants should be optimized against a pool of synthetic spectra (examples) from certain types of problems to guarantee the convergence of the optimization technique for this type of problems. In case of more robust optimization schemes, the tuned *group B* constants are more widely applicable; however, in general *group B constants* should be optimized for each particular class of problems, before the real characterization process is begun.

> Generally, case independence of the convergence quality is one of the important properties of an optimization method.

4.4. Application of Different Optimization Schemes

Various optimization methods can be applied to solve the inverse problem. However, not all are generally efficient in the biosystem characterization process.

Optimization methods can be divided according to two criteria:

- Means of moving through the phase space
- Size of the optimizing set.

Accordingly, four groups of methods can be identified:

- Deterministic – single individual optimization
- Stochastic – single individual optimization
- Deterministic – population optimization
- Stochastic – population optimization

The above method classes are sorted according to their speed, fine-tuning capabilities, and, on the contrary, to the robustness of the method. The fastest methods are deterministic (single individual optimizations), whereas the most robust are stochastic (population optimizations).

The basic scheme of any optimization method includes initialization and the main loop where parameters are changed according to predefined rules. At each evaluation of the main loop the fitness function is checked to fulfill predefined stop criteria. Optimization methods, however, differ in the way each of these steps is performed.

According to the size and partial correlation in phase spaces that can be found in biosystem characterization processes, robustness becomes a much more important issue than speed, although speed can be a limiting factor. To select a robust method, we can search within a class of population-based optimizations that are in general less sensitive to local extremes as well as to model speciations. Optimization methods that do not calculate the spectral derivatives explicitly are especially useful, since the numerical calculation of spectral derivatives is in general a noise-amplifying process.

In our case, evolutionary optimization (i.e., the generational genetic algorithm created by Holland) is taken as a base for inverse problem solving due its robustness and genotype-driven movements in large-phase-space search. This enables a global search independent of detection of local minima. However, due to its inability in terms of fine-tuning, it is efficient to hybridize it with a deterministic method like the Simplex-Downhill "amoeba" of Nelder and Mead — which also does not require a derivative calculation. To get an idea of the implementation, we summarize some important properties below.

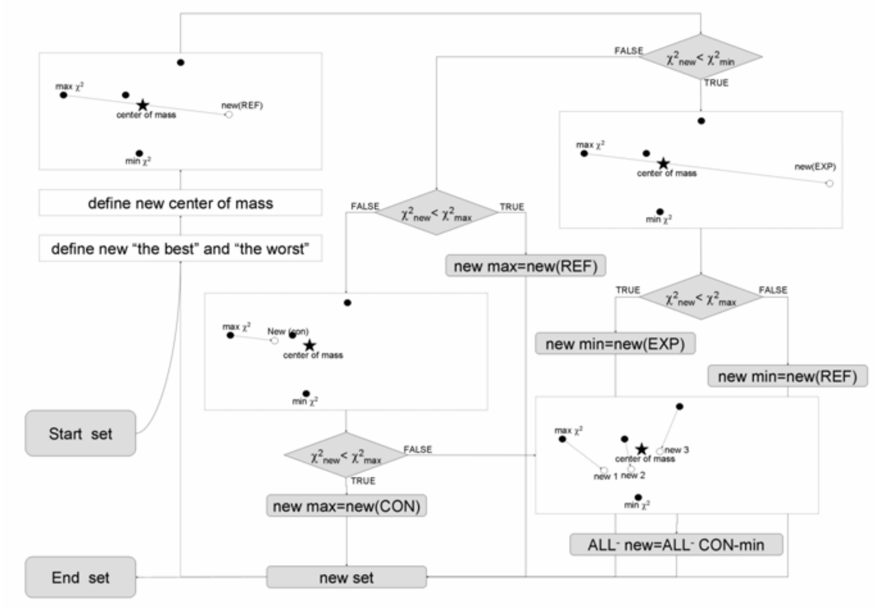

Figure 19. The main loop of SD optimization.

The **Simplex Downhill** (SD) **algorithm** is based on linear transformations of a population of N_p+1 points (each point is a set or vector of all spectral parameters $\{p_i\}$), where N_p is the number of optimizing parameters.

A starting population is usually created from an input vector $\{p_{i,0}\}$ by modifying the *i*th parameter of the *i*th point of the population for a small step δ_i.

The main loop consists of four linear transformations of the worst or all point(s) relative to the center of mass (originally calculated without the worst point; see Figure 19):

- Reflection of the worst point across center of mass
- Reflection of the worst point across center of mass and expansion away
- Contraction of the worst point in the direction of the center of mass
- Contraction of all except the best point toward the best point

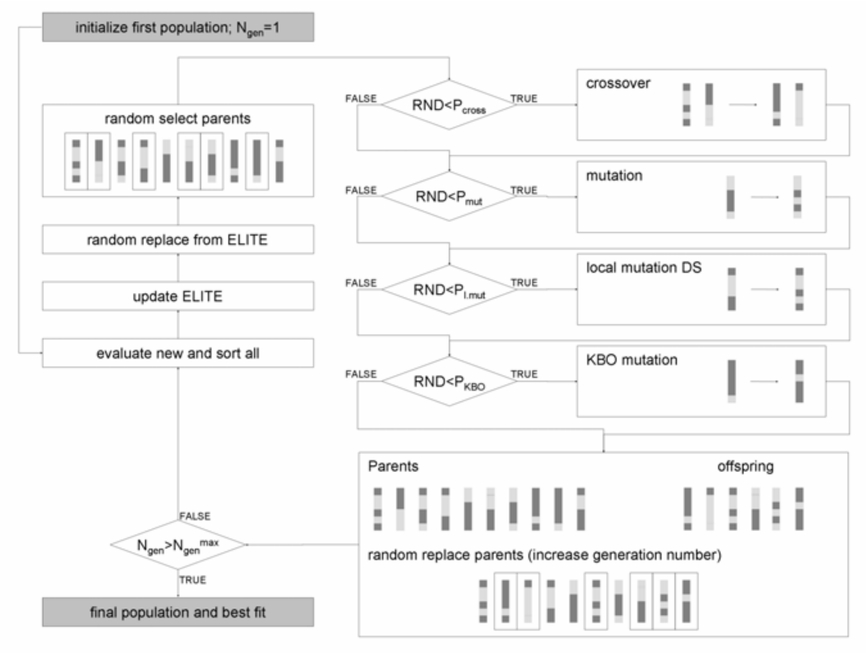

Figure 20. The main loop of **GA (EO)** and **HEO** optimization.

The **generational Genetic (GA) Algorithm** is based on genetic-like transformations of parameters of a large population of M points, where $M \gg N_p$ (each point is a set or vector of spectral parameters $\{p_i\}$), where N_p is the number of optimizing parameters. GA belongs to a family of evolutionary optimization methods; therefore, it is sometimes denoted as EO. When GA is hybridized with a local search operator (like SD) and knowledge-based operators, it is called **Hybrid Evolutionary Optimization** (HEO).

A starting population is usually created randomly within the definition intervals $[p_{i,\min}, p_{i,\max}]$.

The main loop consists of the selection, real coding, and application of genetic operators in the following scheme (see Figure 20):

- Fitness (χ^2) function evaluation for all new individuals

- Sorting
- Elitism implementation
- Fitness-proportional or tournament selection
- Genetic-operations application:
  - ➢ Multi-point/uniform crossover
  - ➢ Uniform mutation
  - ➢ Local mutation (Simplex Downhill in hybrid version)
  - ➢ Knowledge-based operators (in hybrid version)
- Random replacement

Table 4. Comparison of Advantages and Disadvantages of SD and GA

Simplex Downhill	Genetic algorithm
Advantages	
Accurate, able to fine-tune	Robust
Fast	Model independent
Robust	High probability for finding global minimum (minima)
Model independent	No need for any starting points provided by the user
Disadvantages	
Low probability for finding global minima	Slow, computational very demanding
Need for reasonably good starting point provided by the user in order to be efficient	Disability for fine-tuning of the solution

Here are some notes on the implementation of HEO:

- To improve convergence, the evolutionary optimization approach can be combined with a more conservative approach, called **elitism**, which keeps track of the best individuals found so far and does not allow replacement of any member of this "elite" with worse individuals.
- Efficient hybridization can be achieved with implementation of **DS as a local mutation operator,** performed with a very low probability to maintain diversity within the population.
- To help the algorithm override the problem of partial correlations between pairs or group of parameters, **knowledge-based mutation operators** (KBOs) can be applied. These operators swap the values within such a group of partially correlated parameters with a very low probability. In this way the algorithm induces special jumps in a phase space to search for better solutions.

4.5. Accuracy and Reproducibility of Solutions

At the end of the characterization procedure, the solutions have to be classified in terms of reproducibility and accuracy.

Reproducibility is related to the effectiveness, robustness, and fine-tuning ability of the optimization routine, and is defined through:

- Means of moving through the phase space
- Starting point(s) determination process
- Ability for global search
- Ability for local search
- Convergence dependence on simulation model

The reproducibility of the method (and model) can be determined via multi-run optimization of spectral parameters using synthetic (simulated) spectra with known parameter sets and contaminated with a low Gaussian noise level. The synthetic spectrum should be produced with the same model as will be used in the optimization. In case of a multi-run stochastic optimization, the determination of reproducibility is straightforward. However, in case of a multi-run deterministic method, special care should be taken to supply a large set of random starting points. The similarity of the synthetic spectra and experimental spectra assures that the reproducibility is approximately the same when optimization is done with a real experimental spectrum or with a synthetic spectrum (as experimental one).

Accuracy defines the most probable range(s) of a real solution (confidence region). It depends on:

- Signal-to-noise ratio of the experimental data
- Partial correlations between different model parameters

Accuracy can be determined in a straightforward manner using multi-run stochastic optimization methods. The area that includes 66% of the solutions around the averaged solution defines the standard confidence region (in the multidimensional space). However, this region also includes the reproducibility range, which has to be subtracted from this confidence region.

In the case when deterministic methods are used, the accuracy determination is not so reliable. The simplest way is to expand $\chi^2(\{p_i\})$ around an optimized value $\{p_{i,0}\}$ and determine the confidence region through a second derivative matrix α (*Hessian matrix*). Note that this method can be used only as a rough approximation only if the optimized value $\{p_{i,0}\}$ is in a real minimum.

The elements of the Hessian matrix $\alpha_{k,l}$ can be calculated as

$$\alpha_{k,l} = \sum_{j=1}^{N} \frac{1}{\sigma^2} \left(\frac{\partial y_j^{\text{sim}}}{\partial p_k} \frac{\partial y_j^{\text{sim}}}{\partial p_l} \right), \tag{63}$$

where N is the number of points in the spectrum, σ is the standard deviation of the experimental points, p_i are the spectral parameters and y_j^{sim} are the values of the simulated spectra.

The inverse of Hessian matrix α is defined as *covariance matrix C*:

$$C \equiv \alpha^{-1}. \tag{64}$$

The diagonal elements can be used to derive a rough approximation to confidence intervals σ_i:

$$\sigma_i = \sqrt{C_{ii}}\ . \tag{64}$$

The off-diagonal elements approximate correlation coefficients $c_{i,j}$:

$$c_{i,j} = \frac{C_{i,j}}{\sqrt{C_{ii}}\sqrt{C_{jj}}}\ . \tag{66}$$

4.6. Complexity of a Biological System: GHOST Condensation

Before the characterization procedure is applied to determine biosystem complexity, one has to check that the inverse problem is not ill-posed. Frequent divergence or "address violation errors" that are detected within the optimization indicate that the model cannot adequately describe the experimental data or is not sensitive to a certain part of the model phase space (a combination of some parameters in a certain interval). Any of these possibilities calls for immediate model modifications.

However, even if the optimization converges successfully in 100% of cases, there is still a possibility that the model cannot fully describe the experimental system response due to low complexity of the proposed model. This can be recognized by the following features

- Successful convergence with no obvious model errors
- Many equally good solutions provided by the multi-run stochastic optimization routines
- High reproducibility and accurateness of solutions found for the synthetic spectra with the same model and the same optimization routines

In such a case, the appearance of virtual irreproducibility of solutions of real problems results from low **model complexity**.

Often the response of a biosystem is more complex than the simulation model can handle. Consequently, the simulation model cannot lead to a perfect solution, but only to a low-dimensional "projection." Clearly, many good projections exist of the same higher-dimensional object. This fact is implemented in a so-called

GHOST condensation approach based on multiple HEO runs, and to roughly construct a quasi-continuous description of the complex system, even when model complexity is proposed to be finite.

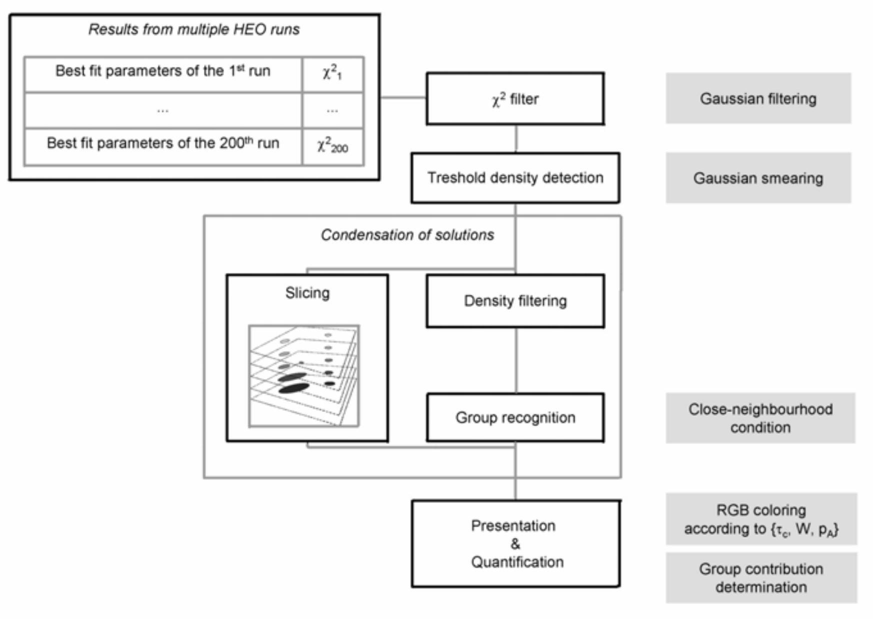

Figure 21. The GHOST approach.

In GHOST condensation, it as assumed that the maximal number of spectral parameters that can be resolved from nitroxide based spectra is between 20 and 30. This corresponds to 4 spectral components. Therefore, a 4-component model is applied in spectral simulation models. The approach is divided into the following four steps (see also Figure 21):

1. **Collection of solutions**: To collect possible projections of the complex system, multiple runs of HEO are performed (up to 200 runs). In an older approach only the best-fit parameter sets of each run were used in the further condensation procedure. However, faster acquisition of solution is obtained by acquiring the best 10 solutions from the population of each run, in combination with new "shaking" operators to maintain solution diversity in a single run (dHEO algorithm).
2. **Filtering of solution**: To assure that only the successful optimization runs were taken into account, 40% of the best-fit sets were passed through the χ^2-filter. In addition, the density of the solutions in the parameter space was calculated to enable density filtering. The latter

is applied to pass through only those solutions that possess a local density higher than the minimum density threshold. With this filter unusual solutions (that are not found in several runs) are thrown away.

3. **Condensation of solutions within a slicing procedure**: Predefined uncertainties of spectral parameters are used to group the solutions according to a neighborhood condition at various density levels. The groups are used to calculate the center of mass of each group of solutions as well as their second moment (spreading of the solution). This is used to discriminate between the discrete and continuous character of a particular group. In addition, slicing by itself can also help to determinate this character: by tracking the center of mass of each group from the highest to the lowest density slice. Discrete groups do not change it center of mass significantly from slice to slice; however, quasi-continuous groups with or without discrete groups superimposed on it can significantly change the center of mass between slices.
4. **GHOST presentation**: The groups of solutions can be presented by two-dimensional cross-section diagrams, such as S–τ_c, S–W, S–p_A, or θ–ϕ, θ–τ_c, θ–W, θ–p_A, depending on the model used (here S, τ_c, W, and p_A represent typical model parameters: order parameter, effective rotational correlation time, additional broadening constant, and polarity correction factor on the hyperfine tensor). In addition, RGB color coding can be applied to enable fast tracking of groups between different GHOST diagrams (see Figure 22).

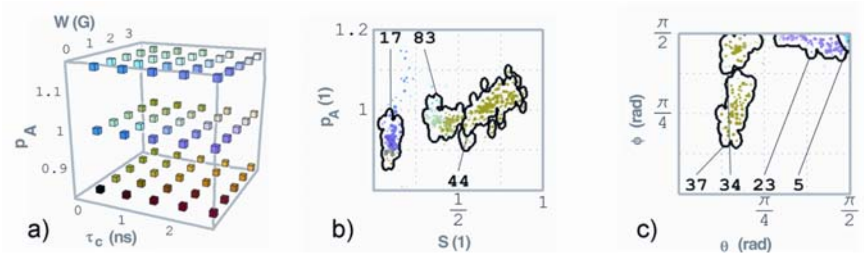

Figure 22.RGB color cube (a) and two examples of GHOST diagrams: MT1 breast cancer cells spin labeled with MeFASL (10,3) growing 5 days at (10.4 ± 1.8) × 10^6 cells in the culture flask (b), and SDSL of M13 coat protein — cysteine mutant spin labeled at position 34 (c).

As can be seen from the examples in Figure 22, the motional/polarity patterns can be recognized for different biosystems under various conditions. In the case of a nonspecifically spin-labeled membrane (b), some sharply defined solutions are found together with a quasi-continuous distribution of solutions. This indicates that a part of the membrane cannot be modeled well (contrary to healthy cells, which usually possess well-resolved discrete domain structure; data not shown). In case of a site-directed spin labeled cysteine mutant of a membrane protein that was reconstituted in a model membrane (c), coexistence of different motional/polarity patterns is observed. This points to coexisting local conformations of this membrane protein with different restrictions and rates of rotational motion, polarity, and interaction with the oxygen (additional broadening), which together with the polarity information indicate the position of the label relative to the membrane surface, i.e., relative to the water and oxygen partitioning profiles.

Many other models and applications can also be involved in the characterization scheme that is presented in this chapter. According to a recent decrease in the numerical demand of this characterization to roughly one spectrum per 1-GFLOPS processor per day and successful elimination of user interaction from the core of this procedure, this approach is affordable now for any spectroscopic laboratory without a huge investment in computer mainframes or computer clusters.

5. APPENDIX

The explicit expressions for the $\underline{\tilde{G}}$ and $\underline{\tilde{A}}$ terms after averaging are given below. Note that the terms involving sin(φ), cos(φ), sin(2φ), sin(ψ), and sin(2ψ) vanish after averaging due to symmetry reasons:

$$\begin{aligned}\tilde{G}_{xx}^{\text{avg}} &= g_{xx}^2\left(\overline{\cos^2(\varphi)}\ \overline{\cos^2(\vartheta)}\ \overline{\cos^2(\psi)}+\overline{\sin^2(\varphi)}\ \overline{\sin^2(\psi)}\right)\\ &\quad+g_{yy}^2\left(\overline{\sin^2(\varphi)}\ \overline{\cos^2(\vartheta)}\ \overline{\cos^2(\psi)}+\overline{\cos^2(\varphi)}\ \overline{\sin^2(\psi)}\right),\\ &\quad+g_{zz}^2\,\overline{\sin^2(\vartheta)}\ \overline{\cos^2(\psi)}\end{aligned} \tag{A.1}$$

$$\begin{aligned}\tilde{G}_{yy}^{\text{avg}} &= g_{xx}^2\left(\overline{\cos^2(\varphi)}\ \overline{\cos^2(\vartheta)}\ \overline{\sin^2(\psi)}+\overline{\sin^2(\varphi)}\ \overline{\cos^2(\psi)}\right)\\ &\quad+g_{yy}^2\left(\overline{\sin^2(\varphi)}\ \overline{\cos^2(\vartheta)}\ \overline{\sin^2(\psi)}+\overline{\cos^2(\varphi)}\ \overline{\cos^2(\psi)}\right),\\ &\quad+g_{zz}^2\,\overline{\sin^2(\vartheta)}\ \overline{\sin^2(\psi)}\end{aligned} \tag{A.2}$$

$$\tilde{G}_{zz}^{\text{avg}} = g_{xx}^2\,\overline{\cos^2(\varphi)}\ \overline{\sin^2(\vartheta)}+g_{yy}^2\,\overline{\sin^2(\varphi)}\ \overline{\sin^2(\vartheta)}+g_{zz}^2\,\overline{\cos^2(\vartheta)}, \tag{A.3}$$

$$\tilde{G}_{xz}^{\text{avg}}=0\,,\ \ \tilde{G}_{xy}^{\text{avg}}=0\,,\ \ \tilde{G}_{yz}^{\text{avg}}=0\,. \tag{A.4–6}$$

Similarly averaged effective hyperfine tensor components are expressed as

$$\begin{aligned}\tilde{A}_{xx}^{\text{avg}} &= \frac{A_{xx}}{g_{xx}^2}\left(\overline{\cos^2(\varphi)}\;\overline{\cos^2(\vartheta)}\;\overline{\cos^2(\psi)}+\overline{\sin^2(\varphi)}\;\overline{\sin^2(\psi)}\right)\\ &+\frac{A_{yy}}{g_{yy}^2}\left(\overline{\sin^2(\varphi)}\;\overline{\cos^2(\vartheta)}\;\overline{\cos^2(\psi)}+\overline{\cos^2(\varphi)}\;\overline{\sin^2(\psi)}\right)\\ &+\frac{A_{zz}}{g_{zz}^2}\overline{\sin^2(\vartheta)}\;\overline{\cos^2(\psi)},\end{aligned}\tag{A.7}$$

$$\begin{aligned}\tilde{A}_{yy}^{\text{avg}} &= \frac{A_{xx}}{g_{xx}^2}\left(\overline{\cos^2(\varphi)}\;\overline{\cos^2(\vartheta)}\;\overline{\sin^2(\psi)}+\overline{\sin^2(\varphi)}\;\overline{\cos^2(\psi)}\right)\\ &+\frac{A_{yy}}{g_{yy}^2}\left(\overline{\sin^2(\varphi)}\;\overline{\cos^2(\vartheta)}\;\overline{\sin^2(\psi)}+\overline{\cos^2(\varphi)}\;\overline{\cos^2(\psi)}\right)\\ &+\frac{A_{zz}}{g_{zz}^2}\overline{\sin^2(\vartheta)}\;\overline{\sin^2(\psi)},\end{aligned}\tag{A.8}$$

$$\tilde{A}_{zz}^{\text{avg}} = \frac{A_{xx}}{g_{xx}^2}\overline{\cos^2(\varphi)}\;\overline{\sin^2(\vartheta)}+\frac{A_{yy}}{g_{yy}^2}\overline{\sin^2(\varphi)}\;\overline{\sin^2(\vartheta)}+\frac{A_{zz}}{g_{zz}^2}\overline{\cos^2(\vartheta)},\tag{A.9}$$

$$\tilde{A}_{xz}^{\text{avg}}=0,\quad \tilde{A}_{xy}^{\text{avg}}=0,\quad \tilde{A}_{yz}^{\text{avg}}=0.\tag{A.10–12}$$

With the above averaged expressions one can define the expressions for the effective tensors g^{eff}, $A_{zz}{}^{\text{eff}}$, $A_{xzyz}{}^{\text{eff}}$, $A_{xyxy}{}^{\text{eff}}$, and $A_{xxyy}{}^{\text{eff}}$ of the final spin Hamiltonian of Eq. (39):

$$\left(g^{\text{eff}}(\Theta_i,\Phi_i)\right)^2=\tilde{G}_{xx}^{\text{avg}}\cos^2(\Phi_i)\sin^2(\Theta_i)+\tilde{G}_{yy}^{\text{avg}}\sin^2(\Phi_i)\sin^2(\Theta_i)+\tilde{G}_{zz}^{\text{avg}}\cos^2(\Theta_i),\tag{A.13}$$

$$\begin{aligned}A_{zz}^{\text{eff}}(\Theta_i,\Phi_i)=[&\tilde{A}_{xx}^{\text{avg}}\cos^2(\Phi_i)\sin^2(\Theta_i)+\tilde{A}_{yy}^{\text{avg}}\sin^2(\Phi_i)\sin^2(\Theta_i)\\ &+\tilde{A}_{zz}^{\text{avg}}\cos^2(\Theta_i)]\left(g^{\text{eff}}(\Theta_i,\Phi_i)\right)^2,\end{aligned}\tag{A.14}$$

$$\begin{aligned}A_{xzyz}^{\text{eff}}(\Theta_i,\Phi_i)=&\left[\frac{1}{2}\left(\tfrac{1}{2}\left(\tilde{A}_{xx}^{\text{avg}}\cos^2(\Phi_i)+\tilde{A}_{yy}^{\text{avg}}\sin^2(\Phi_i)-\tilde{A}_{zz}^{\text{avg}}\right)\sin(2\Theta_i)\right)\right.\\ &\left.+\frac{i}{2}\left(\tfrac{1}{2}\left(\tilde{A}_{xx}^{\text{avg}}-\tilde{A}_{yy}^{\text{avg}}\right)\sin(2\Phi_i)\sin(\Theta_i)\right)\right]\left(g^{\text{eff}}(\Theta_i,\Phi_i)\right)^2,\end{aligned}\tag{A.15}$$

$$\begin{aligned}A_{xyxy}^{\text{eff}}(\Theta_i,\Phi_i)=&\left[\frac{1}{4}\left(\tilde{A}_{xx}^{\text{avg}}\left(\cos^2(\Phi_i)\cos^2(\Theta_i)-\sin^2(\Phi_i)\right)+\tilde{A}_{yy}^{\text{avg}}\left(\sin^2(\Phi_i)\cos^2(\Theta_i)-\cos^2(\Phi_i)\right)\right.\right.\\ &\left.\left.+\tilde{A}_{zz}^{\text{avg}}\sin^2(\Theta_i)\right)\;+\frac{i}{2}\left(\tfrac{1}{2}\left(\tilde{A}_{xx}^{avg}-\tilde{A}_{yy}^{avg}\right)\sin(2\Phi_i)\cos(\Theta_i)\right)\right]\left(g^{\text{eff}}(\Theta_i,\Phi_i)\right)^2,\end{aligned}\tag{A.16}$$

$$\begin{aligned}A_{xxyy}^{\text{eff}}(\Theta_i,\Phi_i)=&\frac{1}{4}\left[\tilde{A}_{xx}^{\text{avg}}\left(1-\cos^2(\Phi_i)\sin^2(\Theta_i)\right)+\tilde{A}_{yy}^{\text{avg}}\left(1-\sin^2(\Phi_i)\sin^2(\Theta_i)\right)+\right.\\ &\left.+\tilde{A}_{zz}^{\text{avg}}\sin^2(\Theta_i)\right]\left(g^{\text{eff}}(\Theta_i,\Phi_i)\right)^2.\end{aligned}\tag{A.17}$$

6. ACKNOWLEDGMENTS

This work is granted by the Slovenian Research Agency (Ministry of Higher Education, Science and Technology, grants P1-0060 and J1-6581). It was also partially supported by the ESF COST D22 action. I wish to thank all my colleagues at the Laboratory of Biophysics at the EPR center, “Jožef Stefan” Institute, in Ljubljana, for many discussions and lots of important notes on this chapter. I am also grateful to Bogdan Filipič, David Stopar, Peter Laggner, and Marcus A. Hemminga, who helped me to evolve this approach to the current situation.

7. INTERESTING REFERENCES AND FURTHER READING

Spin-Labeling ESR Spectroscopy

Arsov Z, Schara MV, Zorko M, Štrancar J. 2004. The membrane lateral domain approach in the studies of lipid–protein interaction of GPI-anchored bovine erythrocyte acetylcholinesterase. *Eur Biophys J* **33**:715–725.

Borbat PP, Costa-Filho AJ, Earle KA, Moscicki JK, Freed JH. 2001. Electron spin resonance in studies of membranes and proteins. *Science* **291**:266–269.

Chiang YW, Shimoyama Y, Feigenson GW, Freed JH. 2004. Dynamic molecular structure of DPPC–DLPC–cholesterol ternary lipid system by spin-label electron spin resonance. *Biophys J* **87**:2483–2496.

Griffith OH, Jost PC. 1976. Lipid spin labels in biological membranes. In *Spin labeling, theory and application*, pp. 453–523. Ed LJ Berliner. New York: Academic Press.

Kurad D, Jeschke G, Marsh D. 2003. Lipid membrane polarity profiles by high-field EPR. *Biophys J* **85**:1025–1033.

Marsh D. 2002. Membrane water-penetration profiles from spin labels. *Eur Biophys J* **31**:559–562.

Rappolt M, Amenitsch H, Štrancar J, Teixeira CV, Kriechbaum M, Pabst G, Majerowicz M, Laggner P. 2004. Phospholipid mesophases at solid interfaces: in-situ X-ray diffraction and spin-label studies. *Adv Colloid Interface Sci* **111**:63–77.

Shin YK, Freed JH. 1989. Dynamic imaging of lateral diffusion by electron spin resonance and study of rotational dynamics in model membranes: effect of cholesterol. *Biophys J* **55**:537–550.

Simulation of ESR Spectra

Della Lunga G, Pezzato M, Baratto MC, Pogni R, Basosi R. 2003. A new program based on stochastic Liouville equation for the analysis of superhyperfine interaction in CW-ESR spectroscopy. *J Magn Reson* **164**:71–77.

Eviatar H, van der Heide UA, Levine YK. 1995. Computer simulations of the electron spin resonance spectra of steroid and fatty acid nitroxide probes in bilayer systems. *J Chem Phys* **102**:3135–3145.

Hemminga MA. 1983. Interpretation of ESR and saturation transfer ESR spectra of spin labeled lipids and membranes. *Chem Phys Lipids* **32**:323–383.

Marsh D. 1981. Electron spin resonance: spin labels. In *Membrane spectroscopy*, pp. 51–142. Ed E Grell. Berlin: Springer.

Schneider DJ, Freed JH. 1989. Calculating slow motional magnetic resonance spectra: a user's guide. In *Biological magnetic resonance: spin labeling, theory and applications*, pp. 1–76. Ed LJ Berliner, J Reuben. New York: Plenum.

Steinhoff HJ, Hubbell WL. 1996. Calculation of electron paramagnetic resonance spectra from Brownian dynamics trajectories: application to nitroxide side chains in proteins. *Biophys J* **71**:2201–2212.

Štrancar J, Sentjurc M, Schara MV. 2000. Fast and accurate characterization of biological membranes by EPR spectra. *J Magn Reson* **142**:254–265.

Van SP, Birrell GB, Griffith OH. 1974. Rapid anisotropic motion of spin labels: models for motion averaging of the ESR parameters. *J Magn Reson* **15**:444–459.

Optimization Methods of ESR Spectral Parameters

Budil DE, Lee S, Saxena S, Freed JH. 1996. Nonlinear-least-squares analysis of slow-motion EPR spectra in one and two dimensions using a modified Levenberg-Marquardt algorithm. *J Magn Reson A* **120**:155–189.

Della Lunga G, Pogni R, Basosi R. 1998. Global versus local minimization procedures for the determination of spin Hamiltonian parameters from electron spin resonance spectra. *Mol Phys* **95**:1275–1281.

Filipič B, Štrancar J. 2003. Evolutionary computational support for the characterization of biological systems. In *Evolutionary computation in bioinformatics*, pp. 279–294. Ed GB Fogel, D Corne. Amsterdam: Elsevier Science.

Filipič B, Štrancar J. 2001. Tuning EPR spectral parameters with a genetic algorithm. *Appl Soft Comp* **1**:83–90.

Kavalenka AA, Filipič B, Hemminga MA, and Štrancar J. 2005. Speeding up a genetic algorithm for EPR-based spin label characterization of biosystem complexity. *J Chem Inf Model* **45**:1628–1635.

Moens P, De Volder P, Hoogewijs R, Callens F, Verbeeck R. 1993. Maximum-likelihood common-factor analysis as a powerful tool in decomposing multicomponent EPR powder spectra. *J Magn Reson A* **101**:1–15.

Evolutionary Optimizations

Eiben AE, Smith JE. 2003. *Introduction to evolutionary computing*. Berlin: Springer.

Goldberg DE. 1989. Genetic algorithms in search, optimization and machine learning. Reading, MA: Addison-Wesley.

Complexity Determination

Stopar D, Štrancar J, Spruijt RB, Hemminga MA. 2005. Exploring the local conformational space of a membrane protein by site-directed spin labeling. *J Chem Inf Model* **45**:1621–1627.

Štrancar J, Koklič T, Arsov Z. 2003. Soft picture of lateral heterogeneity in biomembranes. *J Membr Biol* **196**:135–146.

Štrancar J, Schara MV, Pečar S. 2003. New EPR method for cellular surface characterization. *J Membr Biol* **193**:15–22.

Štrancar J, Koklič T, Arsov Z, Filipič B, Stopar D, Hemminga MA. 2005. Spin label EPR-based characterization of biosystem complexity. *J Chem Inf Model* **45**:394–406.

Author's webpage

Laboratory: http://www.ijs.si/ijs/dept/epr/index.html
Personal: http://www.ijs.si/ijs/dept/epr/Janez.html